Framework Programme (FP) 7
Information and Communication Technologies (ICT)
Specific Targeted Research Project (STREP)

FP7 – 224189

ULTRA
Ultra fast eLectronics for THz Rapid Analysis in compact lab-on-chip applications

Ultra-fast eLectronics for Terahertz Rapid Analysis in compact lab-on-chip applications

Measurement results on first generation Aleph/Gimel transmitter and on-chip transmitter and receiver

Deliverable D2.8

Project Coordinator	Dr. Ing. Lorenzo Tripodi Philips Research Europe		
Start date Project	1 June 2008	**Duration**	42 months
Version	3.0		
Status	Final		
Date of issue	05 October 2011		
Filename	ultra-d2.8-final		

0 DOCUMENT INFO

0.1 AUTHORS

Author	Company	e-mail
Lorenzo Tripodi	Philips Research	Lorenzo.Tripodi@philips.com
Marion Matters	Philips Research	
Xin He	Uppsala University	
Dave van Goor	Philips Research	
Reiner Götzen	microTEC	
Heiko Schäfer	Siegen University	
Anders Rydberg	Uppsala University	
Peter Haring Bolivar	Siegen University	

0.2 DOCUMENT HISTORY

Date	Version	Editor	Change	Status
01/05/2011	1.0	Lorenzo Tripodi	First draft. Written executive summary, introduction and chapter 2.	Draft
22/06/2011	1.0	Lorenzo Tripodi	Chapter 3 including Philips and Uppsala University contribution written.	Draft
08/08/2011	2.0	Lorenzo Tripodi	Added chapter 4 and 6 including Philips and Uppsala University contribution. Revisions made. Conclusion written.	Draft
29/09/2011	3.0	Lorenzo Tripodi	Added chapter 5 containing Siegen University results.	Final

0.3 DOCUMENT KEYDATA

Keywords	FP7-224189 – ULTRA, Deliverable D2.2	
Editor Address data	Name	Dr. Lorenzo Tripodi
	Address	Philips Research Europe
		High Tech Campus 37
		5656AE Eindhoven
		The Netherlands
	Phone	+31-(0)40-2749187
	E-mail	lorenzo.tripodi@philips.com

0.4 DISTRIBUTION LIST

Date	Issue	E- mailer
	Report to EC – Project Officer	INFSO-ICT-224189@ec.europa.eu

Table of Contents

Executive Summary

In this report a set of measurements results of essential building blocks of the final Aleph and Gimel demonstrators is reported.

All the different versions of the designed nonlinear transmission lines have shown functionality, and the meandered NLTLs fabricated with the tape out 2 of December 2009 have been chosen to be used in the transmitter and receiver modules of Aleph and Gimel. Direct test of the NLTLs was limited to 170 GHz by the fact that commercial measurement equipment working above 100 GHz is scarcely available and very expensive. Indirect tests of the lines using the Aleph and Gimel receiver and transmitter on wafer have however shown the NLTL capability to work up to 500 GHz (see section 6).

Aleph transmitter version 0.1, version 0.2 and version 0.3 are functional well above 100 GHz and at least up to 220 GHz (this frequency limit is dictated by external laboratory receiver used in the experiments more than our device itself. Further measurements – that will be described in the final deliverable and have been presented at the Intermediate Review meeting on 5 July 2011 – have demonstrated functionality of our transmitter and receiver modules up to 280 GHz at least). The tests described in this document have shown that version 0.2 and version 0.3 made of the nonlinear transmission line (NLTL) created with the tape-out 1 (TO1) of February 2009 and the off-chip Vivaldi antenna have superior performance compared to version 0.1 which is made of the same NLTL and an on-chip antenna. This result is not trivial due to the large uncertainties related to the on-chip/off-chip connection made in Aleph version 0.2 and version 0.3. Considering the superior performance of the off-chip antenna device, this solution has been adopted also in the final demonstrators.

In this report the imaging capability of Aleph transmitter (TX) version 0.3 is also demonstrated. Images taken at frequencies up to 220 GHz of simple objects such as an RFID or a leaf are shown.

The second generation transmitter based on meandered nonlinear transmission lines (tape-out July 2010) and the receiver using a Schottky diode sampling bridge driven by the nonlinear lines have been tested on wafer, connected together via an attenuator of 10 dB. Generation and detection of ultra wide band signals up to the record frequency of 500 GHz (for CMOS device) has been demonstrated. This second generation transmitter and receiver could be tested together without the assistance of a discrete laboratory receiver. The absence of a discrete laboratory receiver has allowed a test of the ULTRA devices without external limitations in frequency or bandwidth - on the contrary of what has been the case for the first generation transmitters Aleph v 0.1, v 0.2 and v 0.3.

1 Introduction

The measurements results carried out (Philips Research and Uppsala University) on all the versions of the nonlinear transmission lines are summarized in chapter 2.
A version of the Aleph transmitter module, named Aleph v. 0.1, has been created. In this version a nonlinear transmission line of first generation (Philips Research) is connected directly to an on-chip slot antenna (Uppsala University). In chapter 3 test results of Aleph v 0.1 are reported.
A second transmitter module, composed of the nonlinear transmission lines, an external Vivaldi antenna (Uppsala University) and a package (microTEC) has been created during 2009. This transmitter, named Aleph v. 0.2, has been tested (Uppsala University) and the results of the tests are reported in chapter 4.
In chapter 5 further tests (Siegen University) carried out on Aleph v 0.3 (a device very similar to Aleph version 0.2) demonstrating the imaging capability of our ULTRA transmitter are described.

In chapter 6 measurements results (Philips Research) of the sampling bridge designed and fabricated (Philips Research) with the tape-out of July 2010 are reported, along with the first tests carried out (Philips Research) on wafer on the second generation transmitter and receiver coupled together.

2 Measurements NLTLs

2.1 NLTL fabricated with tape-out 1 (Feb. 2009)

A micrograph of the fabricated NLTLs is shown in Figure 1. Details of the NLTLs design are described in deliverables D2.2 and D2.4. Each line is straight and around 7 mm long.

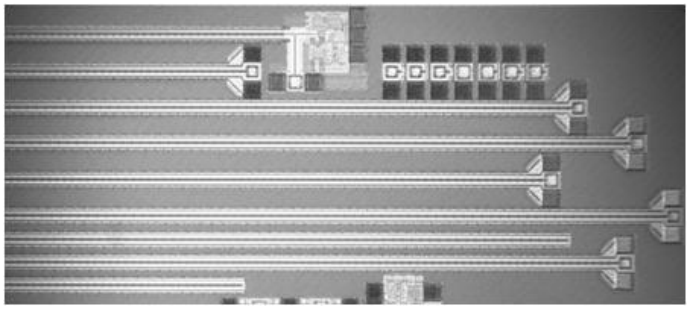

Figure 1 Micrograph of the NLTLs fabricated with tape-out 1 of February 2009.

Small signal, S-parameter measurements were made up to 67 GHz using an Agilent network analyzer type PNA E8361A. Large signal power measurements were carried out in bands. From DC to 50 GHz an Agilent input signal generator type PSG E8257D and a 50 GHz Agilent spectrum analyzer type PSA E4448A were used. Adding to the setup an Agilent mixer type 11970V it was possible to measure in the band from 50 GHz to 67 GHz. From the raw measurement of the available power at the generator and measured power at the spectrum analyzer the actual power at the input and the output of the line under test can be calculated if the losses of the system are known. In the band from 78 GHz to 168 GHz, the output spectrum was measured using an Agilent spectrum analyzer type E4440A with an Agilent harmonic mixer type 11970W (78-108 GHz), and a Pacific Millimeter Products (PMP) harmonic mixer DM connected with a diplexer type MD1A (114 GHz – 168 GHz). The conversion loss of the PMP harmonic mixer was calibrated using a WR-6 band signal source, a WR-6 band attenuator, an Agilent spectrum analyzer type PSA E4440A, and a sub-millimeter power meter Erickson type PM2. The insertion losses of the RF input cable and input Cascade Microtech Infinity probe (I67-75-S) were compensated. An Anritsu RF/Microwave signal generator type MG3694A has been used. In all the power measurements the power actually entering the lines was 18 dBm at 6 GHz.

Figure 2 shows the combined large signal measurements compared with simulations. In simulations, the input signal chosen is a sinusoid with 2.5 V peak voltage at the input of the line. Due to matching, the signal before the source impedance is 5 V peak. This corresponds to an input power of 18 dBm on the 50 Ω-matched line. In measurements the following procedure to de-embed cable losses has been used. In the 6 GHz-66 GHz band an on-chip thru has been used to determine the losses of the cables, the connectors and the probes. Because the length of the thru on chip is only 200 µm, a small length compared to the millimeters-long NLTLs, and because everything is well matched at 50 Ω it is possible to determine with good precision the losses that the signal experiences before the input of the NLTLs and after the output. The measured losses of one cable plus probe are around 2 dB at 6 GHz and 9 dB at 66 GHz. The conversion losses of the mixer were automatically corrected by the spectrum analyzer using data from the manufacturer. In the 78 GHz – 168 GHz range, the insertion loss of the output probe and the conversion loss of the harmonic mixers (shown in Table 1) have been compensated in the measured output power. As it is

clear from Figure 2, simulations (with an estimated stray capacitance equal to 2 fF) and measurements match very well up to 156 GHz. At higher frequencies the match is less good. In Figure 3 it is shown that, as expected from simulation, by tuning at the end of the line the bias voltage of the varactors it is possible to optimize the performance (i.e. the output power at high frequency) of the NLTLs. This is due to the fact that, by changing the bias, the nonlinearity of the varactors is better exploited by the signal swing.

Table 1 Conversion loss of the harmonic mixers: Agilent 11970W (78-108 GHz), and PMP harmonic mixer DM (114 GHz-168 GHz) connected with a diplexer MD1A

Frequency (GHz)	78	84	90	96	102	108	114	120
Conversion Loss (dB)	38	38	39	40	40	41	55	49
Frequency (GHz)	126	132	138	144	150	156	162	168
Conversion Loss (dB)	56	54	51	54	51	52	59	59

The best result is obtained for a bias of -0.5 V, with an improvement of more than 11 dB obtained at 168 GHz with -0.5 V bias compared to the case with +0.5 V bias. It is important to stress that the adverse effect of the output pads has not been de-embedded for the power measurements.

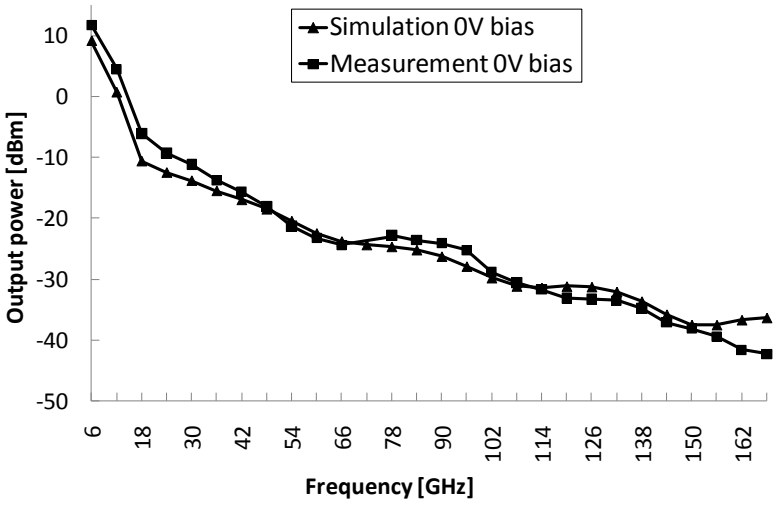

Figure 2 Measured vs. simulated output power of the NLTL. Input frequency and input power are 6 GHz and 18 dBm. The lines are added as a guide for the eye. The power is generated only at the harmonics of 6 GHz indicated by the points.

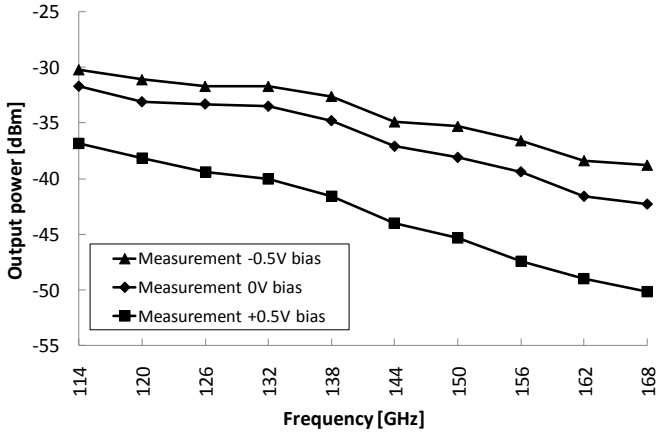

Figure 3 Measured output power for different biasing condition of the NLTL. Input frequency and input power are 6 GHz and 18 dBm.

2.2 NLTLs fabricated with tape-out 2 (Dec. 2009)

The nonlinear transmission lines (NLTLs) designed and fabricated during the second year of the project life (tape-out 2 of December 2009) have been measured and tested during the second and the beginning of the third year of activity. The measurements carried out during the second year have allowed the consortium to verify the NLTL functionality and their suitability for use as building blocks of the final Aleph/Gimel transceiver fabricated with the tapeout of July 2010.

Several different line types have been implemented, as described in PPR2. Here a selection of some important measurement results is reported. The tests described in this section have been effectuated with a setup equal to that one described in section 2.1.

Compared to the first generation lines, the three lines described in this section have a shorter length to reduce chip area and cost. One of the line (type 1, see PPR2 for details) comes in two flavours. The first flavour (type1s) is essentially a copy of the first generation line but with a shorter length (about 5 mm instead of 7 mm). This line has been added here for reference and to check the improvement of the other lines over it. The second flavour (type1m) has the same structure and length of line type 1s but in addition is meandered instead of being straight (see Figure 4). This modification is crucial to allow a compact and low-cost design of the final receiver. The last line (type 2, see PPR2 for details) is straight and its length has been shorten as said before. In addition, also a special floating structure of the metal layers composing the line has been adopted.

In Figure 5 a comparison of the output signal spectrum generated by the three lines is shown. The meandered and the straight line type1s and type1m show similar performance. This result is important because it shows that bending the line to make it more compact degrade only marginally the output power. Meandered lines can

then be used in the final demonstrators to minimize their size and costs. If a high aspect ratio can be tolerated at least in the transmitter, the option to use the straight line 23 of TO1 in that block could be considered if a higher performance is required.

The performance of Line Type2 is also reported on the same figure. As expected from simulations, this line shows a higher output power than lines type1 demonstrating that the floating structure in the metal shield brings substantial improvement over line type1s and type1m. More specifically, the power generated is almost as high as line type 23 (TO1), which was 2 mm longer and hence more expensive. A comparison between line type1s (which is around 5 mm long) and line type 23 (which is 7 mm long) shows another interesting, but unexpected, result. The optimal line length is closer to 7 mm than to 5 mm which was the optimal length calculated optimizing in simulation the output signal fall time. As shown above, this loss of power can be recovered using a floating line structure and should always be evaluated against the substantial gain in chip area and cost achieved reducing the line length from 7 mm to 5 mm.

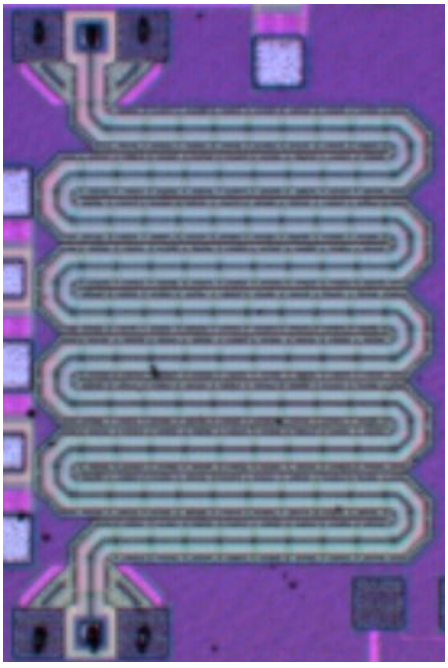

Figure 4 Non linear transmission line type 1 meandered (type1m). This is the line used to implement Aleph and Gimel's transmitter and receiver in tape-out 3 (July 2010).

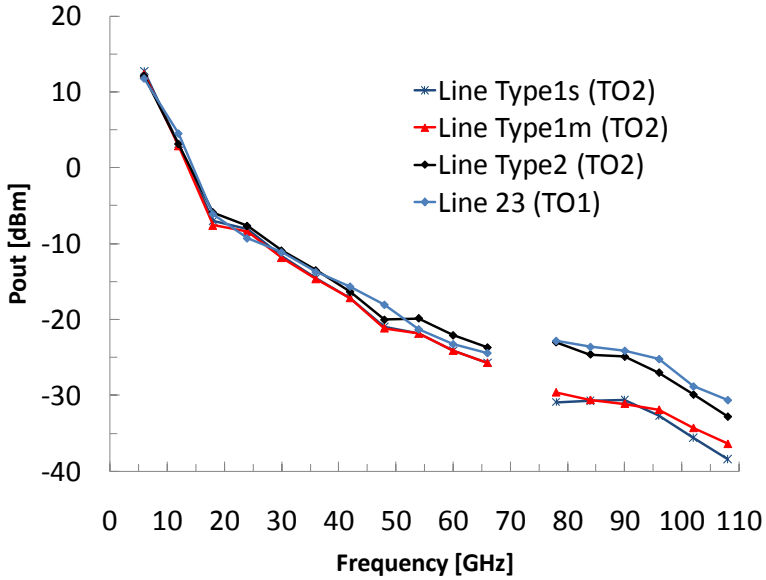

Figure 5 Comparison of the three NLTLs types.

2.3 NLTLs fabricated with tape-out 3 (July 2010)

In the tape out carried out in July 2010 (TO3) a line type 1m has been used to implement the transmitter and the receiver block of Aleph and Gimel. Beside this line, a new type of line has been also designed and fabricated to check if the performance of the previous devices could be further improved. Details of this line are reported in deliverable D2.6. This new NLTL is meandered and has a new floating structure, more complex than line type1m. In Figure 7 a picture photograph of the nonlinear transmission line is reported (bottom side of the figure). In the same figure a linear transmission line (top side of the figure) obtained by the nonlinear transmission line eliminating the varactors is also reported. The latter line is used to test the losses and the matching of the linear part of the nonlinear transmission line.

The tests described in this section have been effectuated with a setup equal to that one described in 2.1.

Figure 7 shows the output power generated by the NLTL when a signal at 6 GHz is injected at its input. Different curves in the graph correspond to different input powers. Comparing the results shown in Figure 5 and in Figure 7 (see Figure 8) it can be seen that, although there is an improvement over line type 1m, this is only marginal. The characteristic impedance of the NLTL is reported in Figure 9 and good matching to 50 Ohms is demonstrated.

In the case of output power and matching measurements, the results fit relatively well with the simulations, but the agreement is somewhat less good than for previous generation lines. The overall performance improvement of the tape-out 3 NLTL is only marginal compared to previous meandered NLTL of tape-out 2.

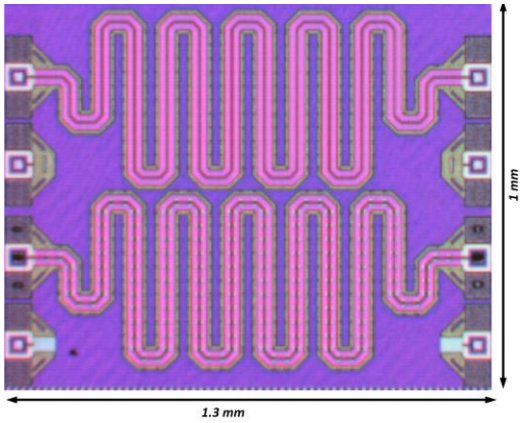

Figure 6 Chip microphotograph of the NLTL (bottom) and the associated LTL (top) fabricated in TO3 (July 2010).

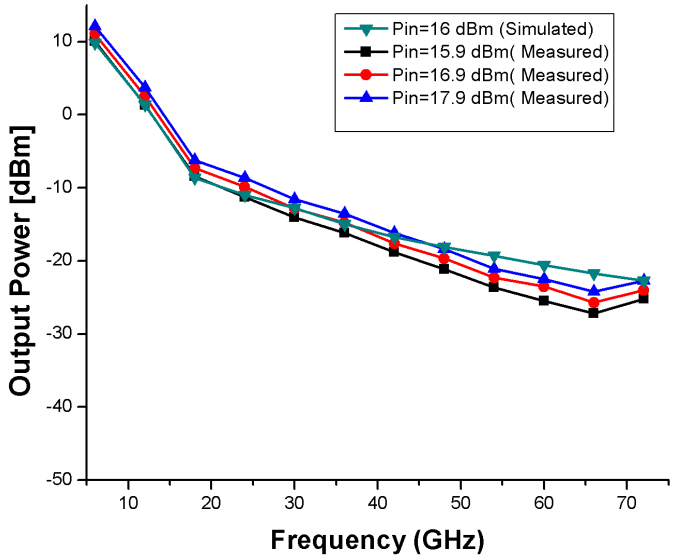

Figure 7 Measured output power of the NLTL (TO3) versus input power and frequency. Input signal is at 6 GHz.

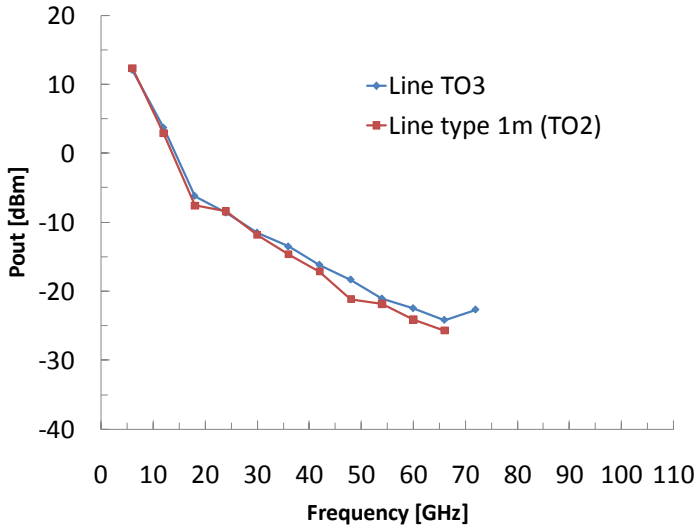

Figure 8 Comparison of the performance of the NLTL of TO3 and the NLTL type 1m fabricated with TO2.

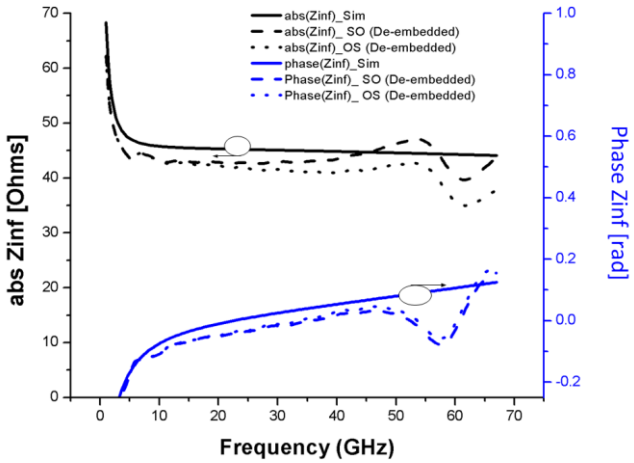

Figure 9 Characteristic impedance of the NLTL fabricated in TO3.

3 Aleph/Gimel transmitter module version 0.1: measurement results

3.1 Module Description

The Aleph transmitter (TX) module version 0.1 is made of a nonlinear transmission line (NLTL) created with tape-out 1 (TO1, February 2009) and an on-chip antenna. The NLTL is a linear transmission line periodically loaded with varactors and it is used to generate a set of higher harmonics from a sinusoidal input signal. A micrograph of several NLTLs fabricated in February 2009 in 65-nm TSMC CMOS technology, one of which is integrated with the EWB antenna forming the Aleph TX module version 0.1, is shown in Figure 10(a). The NLTL in the THz transmitter (i.e., NLTL integrated with the EWB antenna) is 7.1 mm long and it is composed of 190 sections of 37.4 μm long linear transmission lines periodically loaded with voltage-dependent capacitances (Figure 10(b)). As standard coplanar waveguides (CPWs, typically used for the implementation of NLTL in GaAs) are not suitable for CMOS implementation due to the large losses introduced by the low-resistivity silicon substrate, the linear transmission line used to feed the antenna in our design is a modified CPW (m-CPW, as shown in the Figure 10(c)), which is shielded both laterally and from the substrate below with copper to confine the signal in the back-end and to decrease losses. In our design, the nonlinear capacitances are made of CMOS RF varactors type n+-poly/n-well, and the size of the varactors is optimized to achieve a minimum fall time of the output signal in the simulation. After optimization, each varactor has a large signal capacitance of 6.1 fF and an overall capacitance swing of 6 fF when the voltage across its terminals varies from V_L=-2V to V_H=2V. With the variable capacitances used, the falling edge of a low frequency input sinusoid signal is progressively sharpened and harmonics are generated up to sub-terahertz and terahertz waves. The antenna connected with the NLTL has an impedance R_A and transfers power i^2R_A from the circuit as THz radiation. If the output power is sufficient, the signal generated in this way has an extremely wide band spectrum that can be used to carry out THz spectroscopy.
To couple efficiently the free space THz waves to the electrical circuit or vice versa, a suitably designed antenna is required. To characterize its performance, an extremely wideband (EWB) antenna fed by a linear transmission line is fabricated on the same chip as the NLTL, and its micrograph is shown in Figure 11. Figure 11 also gives the schematic of the EWB antenna. To achieve high efficiency, the input impedance of the EWB antenna is designed to be matched to that of the NLTL, which is 50 Ohms. The antenna integrated with the NLTL on a single CMOS chip is fabricated on a 150 μm thick low resistivity (10 Ω▪cm) silicon substrate. The top aluminum metal layer is used to realize the inner stub of the slot antenna, see Figure 11. The radiating slot is in the shape of a wine glass, in which the inner stub is formed by a radial stub with radius Rin = 250 μm, and a rectangle stub with length L = 250 μm and width W= 500 μm. The slot width G is 25 μm. The size of the surrounding ground plane is 1.035mm (L_T) ×0.75mm (W_T).

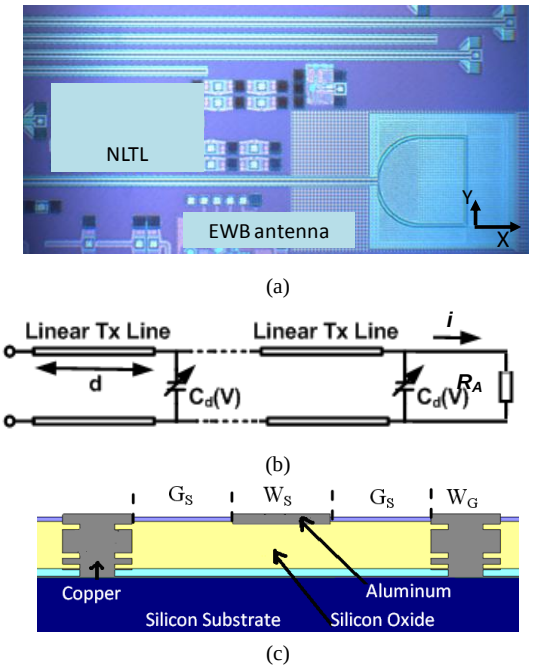

Figure 10 (a) Micrograph of several fabricated NLTLs and of the Aleph transmitter version 0.1 (NLTL+patch antenna); (b) General schematic of the NLTL integrated with EWB antenna; (c) cross section of the modified CPW.

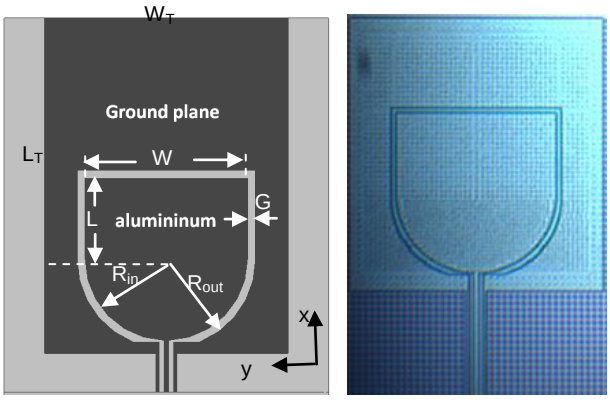

Figure 11 Schematic (left) and micrograph (right) of the EWB antenna.

3.2 Measurements results

On wafer probe measurements in WR-10 and WR-3 bands are carried out. Figure 12 shows the simulated and measured return loss of the antenna. Measurement indicates an adequate 50 Ohm impedance matching (S11<-10 dB) for the band 220 to 300 GHz, which agrees with HFSS simulation result where the antenna exhibits a broad impedance bandwidth of 120-350 GHz.

The simulated normalized gain radiation patterns of the EWB antenna in the frequency range from 100 GHz to 250GHz are given in Figure 13. The antenna features omnidirectional radiation patterns over this frequency range. Due to the fact that the antenna's radiation characteristics suffer from high losses and unwanted substrate modes in the thick low resistivity silicon substrate, numerical results indicate that a radiation efficiency of 44% (at 100 GHz), 31% (at 150 GHz), and 15% (at 200GHz) is achieved.

A measurement of the transmitter has been carried out in two bands, WR-10 and WR-6 bands. The input signal injected into the NLTL is generated from an Anritsu Signal generator MG3694A, and the power level is 18 dBm at 6 GHz and 10 GHz. For receiving, a standard horn antenna is placed under the on-chip antenna silicon substrate at a distance d. In the WR-10 band, an Agilent spectrum analyzer E4440B with an Agilent 11970W harmonic mixer is applied to measure the output spectrum. In the WR-6 band, the Agilent 11970W harmonic mixer is replaced by a Pacific Millimeter Products (PMP) harmonic mixer DM connected with a diplexer MD1A.

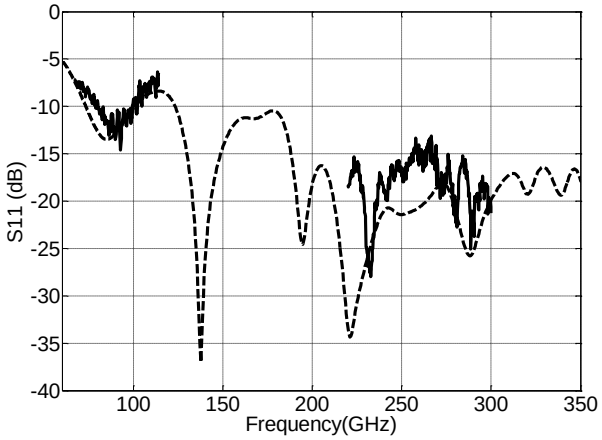

Figure 12 Simulated (dashed line) and measured (solid line) return loss of the EWB antenna.

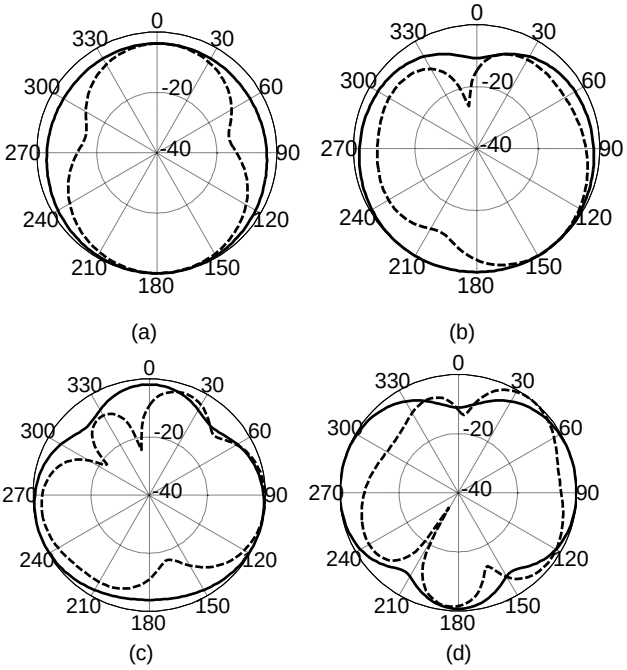

Figure 13 Simulated radiation patterns of the EWB antenna at (a) 100GHz, (b) 150 GHz, (c) 200 GHz, and (d) 250 GHz. Solid line indicates the YZ plane, and dash line indicates the XZ plane.

The measurement of the output power of NLTL alone has also been carried out. Figure 14 shows the received power when the distance d between the standard horn antenna and EWB antenna is 10cm.

The power gain of the antenna is measured on chip with the setup described above. The distance d is changed to 20cm to satisfy the far-field condition, which is equal to or greater than $2D2/\lambda 0$, where D and $\lambda 0$ are the largest aperture dimensions of the antennas and the free-space wavelength at the operating frequency, respectively. From the Friis power

transmission formula, the power received by the horn antenna from the transmitter can be expressed by

$$P_{Transmitter} = P_{NLTL} G_{EWB} G_{Horn} \left(\frac{\lambda}{4\pi d} \right)^2$$

where P_{NLTL} is the output power from NLTL alone, G_{EWB} and G_{HORN} is the gain of the EWB antenna and the horn antenna, respectively, and λ is the wavelength. From the equation, we can derive the approximate gain of the antenna in -Z direction, where samples can be placed in a spectroscopy/imaging application. The result is given in Figure 15, where the derived gain of the EWB antenna shows a maximum value of -9.5 dBi between 90 GHz and 120 GHz. The power radiated from the sub-THz transmitter can be improved increasing the gain of the EWB antenna via adding a low-loss lens, e.g. high resistivity silicon or quartz lens, and/or by removing a major part of the silicon substrate below the antenna.

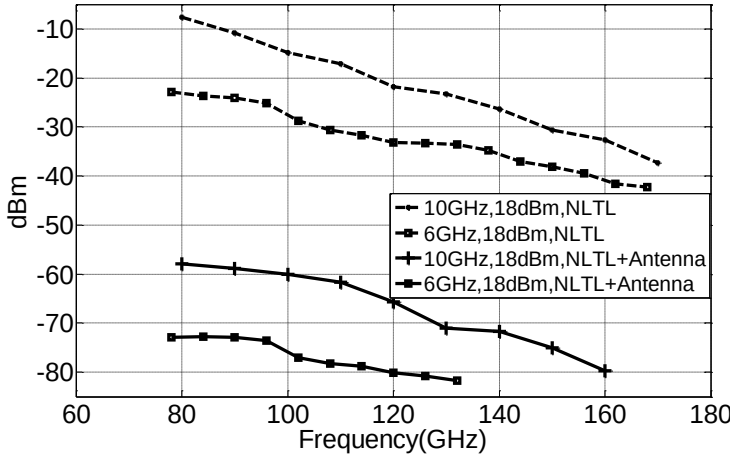

Figure 14 Measured output power of the NLTL alone and of the transmitter (NLTL plus antenna). The power is measured only at the harmonics of 6 GHz/10GHz indicated by the points. The lines are added as a guide for the eye. The distance between the Aleph TX module version 0.1 and the receiver antenna is 10 cm.

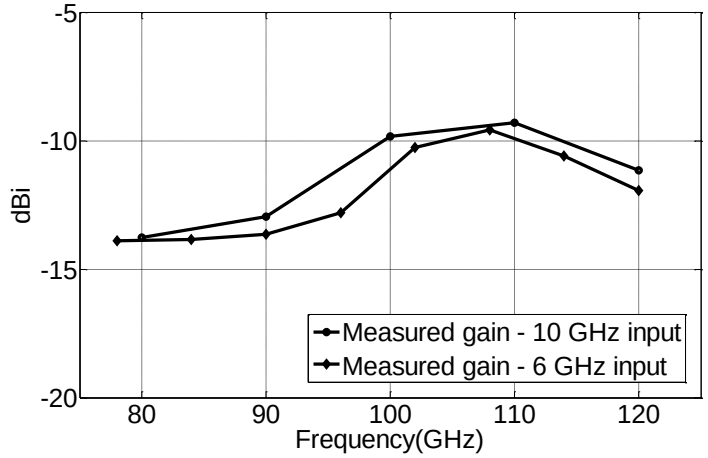

Figure 15 Calculated gain from the measured output power and the simulated gain of the antenna in –Z direction. The input signal of the NLTL is 18 dBm at 6 GHz and 10 GHz.

In summary, the measurements reported in this section have demonstrated the capability of the Aleph transmitter version 0.1 to generate extremely wide-band signals from 78 GHz to

160 GHz at least. The maximum frequency is limited more by the laboratory instrumentation available than the ULTRA device itself. These very good results will be compared in next section with the results obtained with Aleph version 0.2 to determine which is the best solution to choose between a device with an on-chip antenna and one with an off-chip antenna.

4 Aleph/Gimel transmitter module version 0.2: measurement results

4.1 Module Description

The module described in this section (see Figure 16) is composed of a NLTL from TO1 (February 2009) connected with an off-chip Vivaldi antenna and placed in a polymer package. The NLTL is identical to that one discussed in chapter 2. The off-chip Vivaldi antenna has been chosen to avoid the losses of the CMOS substrate and to minimize cost saving expensive CMOS area. As shown in Figure 17(a), the broadband antenna consists of a gradual transition from a microstrip line to a broadside coupled line, followed by a flared slot formed by two identical elliptical tapers.

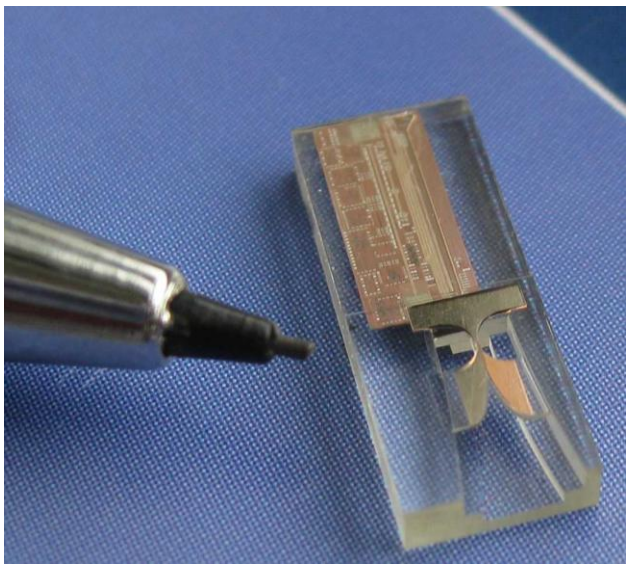

Figure 16 Photograph of Aleph transmitter module version 0.2.

The input impedance of the antenna is designed to match the 50 Ω characteristic impedance of the NLTL. The width of the open slot is W_r = 1.75 mm, the radius of the gradual transition is R = 0.839 mm, and the length of the slot taper is a = 2.75 mm. The length of the microstrip line is 0.571 mm, with centre conductor width of 0.072 mm. The antenna is manufactured on two polymer membranes (so called RMPD® layers, ε_r=2.6) for support and contains integrated air cavities to reduce the dielectric loss in the polymer substrate. Low-loss interconnects at millimetre wave and THz frequencies are crucial for the hybrid solution adopted in this work. Although various techniques, e.g. hot-via and embedded thin die have been successfully demonstrated at lower millimetre wave frequencies, interconnects at frequencies higher than 100 GHz have not been reported in literature yet. In this paper, the antenna is connected to the NLTL line through micro-vias using a 3D chip-scale technology, as shown in Figure 17(b). This technology allows the production of microparts and microsystems without tooling, using a parallel, batch production process on substrates up to 14'' [13]-[15]. In the structure described here, the ground plane of the CMOS NLTL is connected with two vias to the groundplane of the microstrip line in the polymer package. Another via connects the center conductor of the CMOS NLTL to the signal conductor of the microstrip line. The vias pass through a polymer layer H_c on top of the CMOS chip and subsequently through an air gap H. This air gap minimizes the dielectric losses. The thickness of the upper polymer membrane is H_m = 100 µm.

Simulations have been performed to study the RF behaviour of the interconnects as well as the impedance matching and the radiation pattern of the antenna. As shown in Figure 18(a), the reflection and transmission coefficients of the interconnects between the CMOS chip and the antenna indicate that a relatively low-loss transition up to 300 GHz is realized. As shown in Figure 18(b), the off-chip

antenna achieves a simulated impedance bandwidth (S11< -10 dB) of 160-700 GHz. At lower frequencies the matching is less good. This can be improved by lengthening the slot taper.

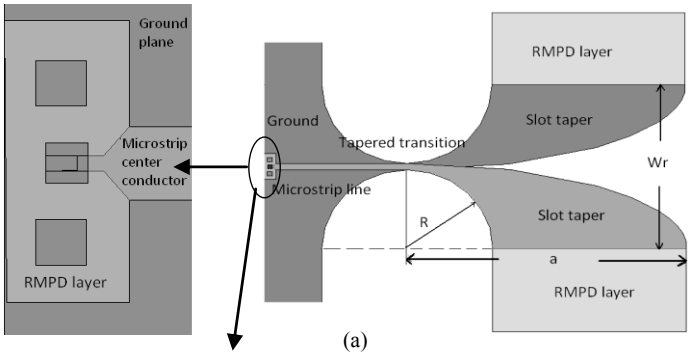

(a)

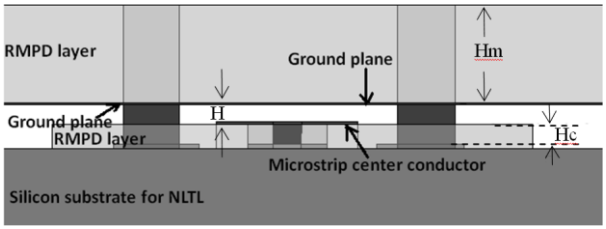

(b)

Figure 17 Details of the off-chip Vivaldi antenna design. (a) Bottom view of the off-chip antenna and detailed view of the transition, (b) detailed cross-section of the transition between the NLTL and the microstrip line embedded in the polymer package, displaying the location of the vias and metal layers (dark-grey) and the polymer layers (light grey) as well as the air gap on top of the CMOS substrate.

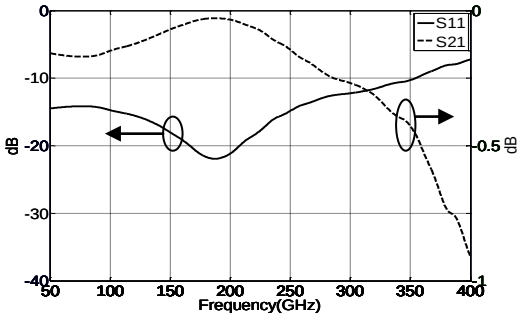

(a)

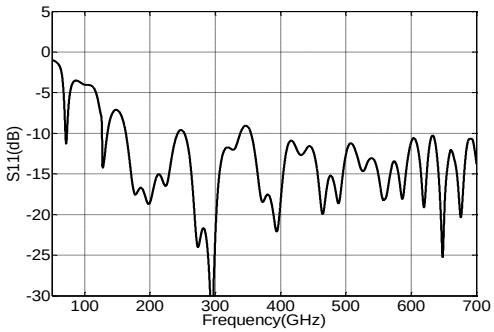

(b)

Figure 18 (a) Simulated reflection and transmission coefficient of the via interconnect between the NLTL on the CMOS chip and the antenna in the polymer package, (b) simulated impedance matching of the antenna.

4.2 Measurements results

The radiated output power as well as the antenna radiation pattern are measured in the WR-10 and WR-6 band with the setup shown in Figure 19. An RF/Microwave signal generator Anritsu MG3694A feeds the nonlinear transmission line through a Cascade Microtech Infinity probe (I67-GSG-75) with a signal at 10 GHz and 18 dBm power. Standard horn antennas for WR-10 (Flan 27240-20, with a mid-band gain of 20 dB) and WR-6 (Quinstar QWH-DPRR00, with a mid-band gain of 24 dB) bands are used to receive the power at a distance *D* from the transmitter module.

In the WR-10 band the output spectrum is measured with an Agilent spectrum analyzer E4440A plus an Agilent 11970W harmonic mixer. In the WR-6 band a PMP harmonic mixer DM connected with a diplexer MD1A is used.

Figure 20 shows the simulated and measured co-polarization normalized gain radiation pattern of the broadband antenna at 90 GHz, 120 GHz and 150 GHz. The antenna features directive radiation patterns over the entire frequency range. Due to the presence of the polymer package below the antenna and the CMOS die, the pattern is tilted away from the end-fire direction in the H plane. Numerical results indicate that a radiation efficiency of more than 70% is achieved.

Figure 21 shows the measured output power of the standalone NLTL, and the radiated power in the end-fire direction of the transmitter. The radiated power is measured at 10 cm, 20 cm and 30 cm distances from the Vivaldi antenna in the end-fire direction. Although the antenna matching is rather poor in the measured frequency band, a power above -80.3 dBm (gain of the receiving antenna is not de-embedded) has been measured up to 170 GHz at 30 cm distance. It should be also remarked that only a fraction of the total power generated by the NLTL is measured in the end-fire direction (the free space losses are, at this frequency and distance, around 67 dB). As shown in Figure 20(c), the measured normalized gain radiation pattern agrees with the simulation results very well, so the total power emitted at 150 GHz can be estimated by integrating the power over all directions according to the simulated full-sphere radiation pattern.

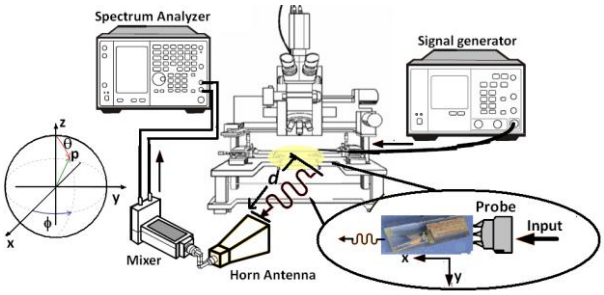

Figure 19 Experimental setup used to measure the Aleph TX module's (version 0.2) output power and the radiation pattern of the off-chip Vivaldi antenna.

With an input signal at 10 GHz and 18 dBm power, the resulting simulated power at 150 GHz is -35.3 dBm, i.e. around -4.7 dB less than the power generated at the same frequency by the stand-alone NLTL. The difference is mostly due to three effects: the losses of the chip-antenna interconnect, the antenna mismatch, and the antenna radiation efficiency. Depending on the final application, and if higher power is especially required at lower frequencies, the impedance matching of the antenna below 110 GHz can be optimized further by utilizing a larger antenna. The gain of the antenna could be improved by adding a low-loss lens in front of the slot taper. Due to the lack of instrumentation the measurements have been carried out only up to 170 GHz, the system is, however, expected to work well beyond that frequency. This is the reason why an antenna with a compact size has been designed with good matching at higher frequencies.

The results of Figure 21 (power measured at 10 cm distance) of Aleph TX version 0.2 (with off-chip antenna) can be directly compared with the results of Figure 14 because the measurements have been taken in the same experimental conditions. From this it is clear that: 1) the connection between the on-chip NLTL and the off-chip antenna is successfully implemented in Aleph TX v. 0.2 and 2) The hybrid module outperforms the monolithic one by 8 dB or more in terms of generated output power in

almost the whole measurement band. This is the reason why, for the final demonstrators an off-chip antenna solution is chosen.

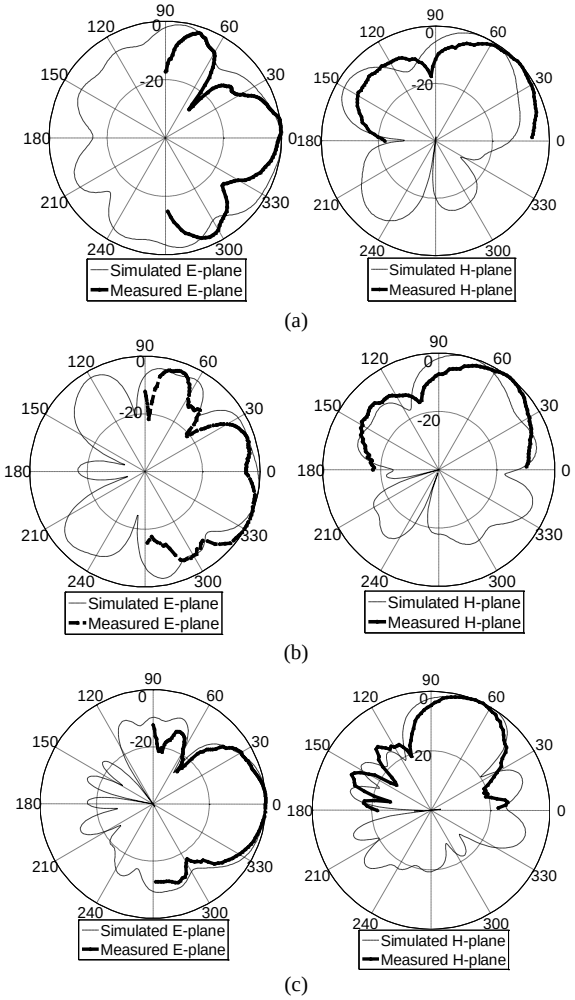

Figure 20 Simulated and measured co-polarization normalized gain radiation patterns in E- and H- plane of the antenna at (a) 90 GHz, (b) 120 GHz, and (c) 150 GHz.

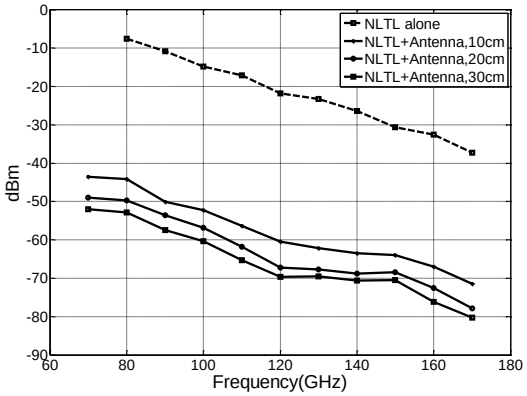

Figure 21 Measured output power of the stand-alone NLTL and the radiated power in the end-fire direction of the hybrid transmitter module at distances D equal to 10 cm, 20 cm and 30 cm. The input power is 18 dBm at 10 GHz.

5 Aleph/Gimel transmitter module version 0.3: imaging capability demonstrated

5.1 Module description

The transmitter module version 0.3 is basically equal to transmitter module version 0.2 (Figure 16), except for a thin air gap present in the Vivaldi antenna of version 0.3. This air gap is used to slightly reduce resistive losses in the package around the antenna structure.

5.2 Measurements and imaging results

The aim of the measurements was to demonstrate the usability of the Aleph transmitter version 0.3 for imaging applications. A picture of the laboratory measurements setup employed is shown in Figure 22. On the left of the figure the Aleph transmitter is placed on a support to allow easy connection of the device to a microprobe and an external generator. On the right of the figure a commercial narrow band antenna collect the radiation sent by the transmitter. The received signal is downconverted by a commercial mixer and measured with a low-frequency spectrum analyzer. The sample under test is placed between two focusing lenses and it is mounted on a XY translation stage to obtain a 2D image in transmission mode. The distance between the transmitter and the receiver is around 40 cm. A magnified view of the measurement setup is reported in Figure 23.

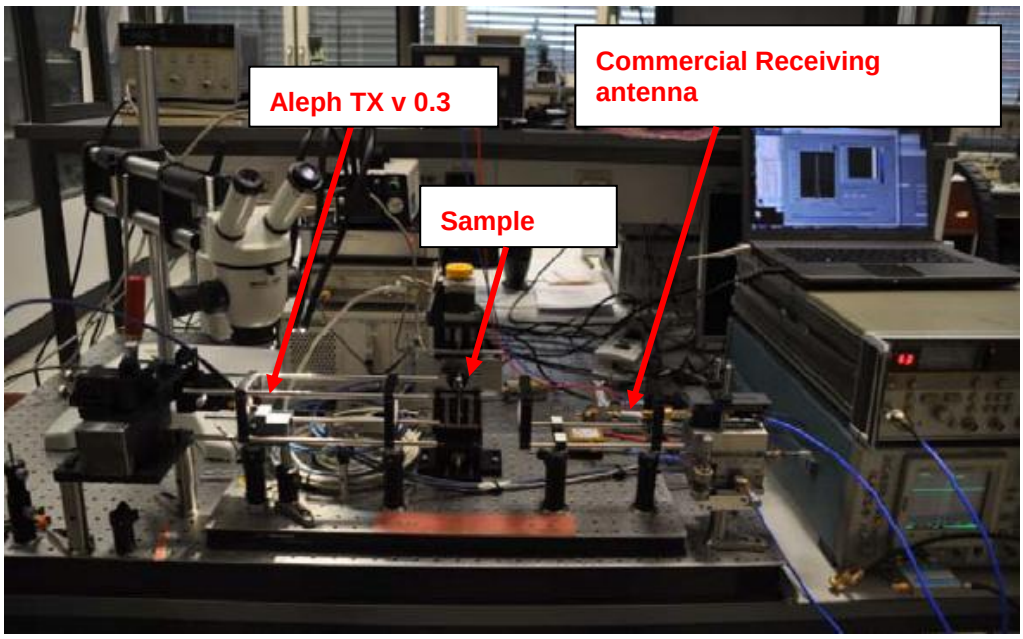

Figure 22 Aleph TX v. 0.3 setup for imaging.

Due to the limited antenna bandwidth of the commercial receiver only few of the harmonics generated by the Aleph transmitter can actually be detected and used to generate an image.

Different objects have been used in the experiment. Figure 24 shows the images of the internal structure of an RFID key obtained at two different frequencies (180 and 220 GHz). The result compares well with the visible image of the unpackaged device. Figure 25 shows two other images of different objects. Finally, Figure 26 shows the image of a freshly cut leaf and the different transmission values of zones with high and low water content is clearly visible.

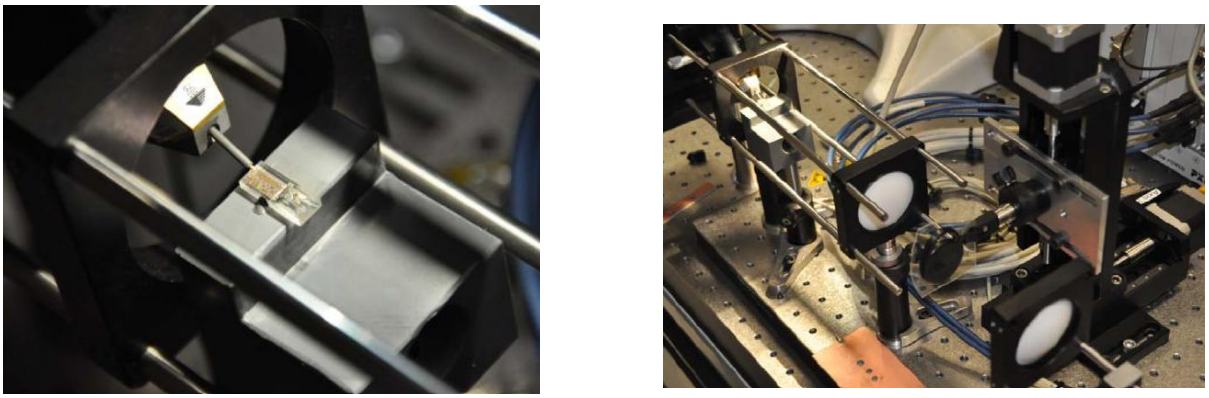

Figure 23 The Aleph THz transmitter (left) and a detail of the whole measurement setup.

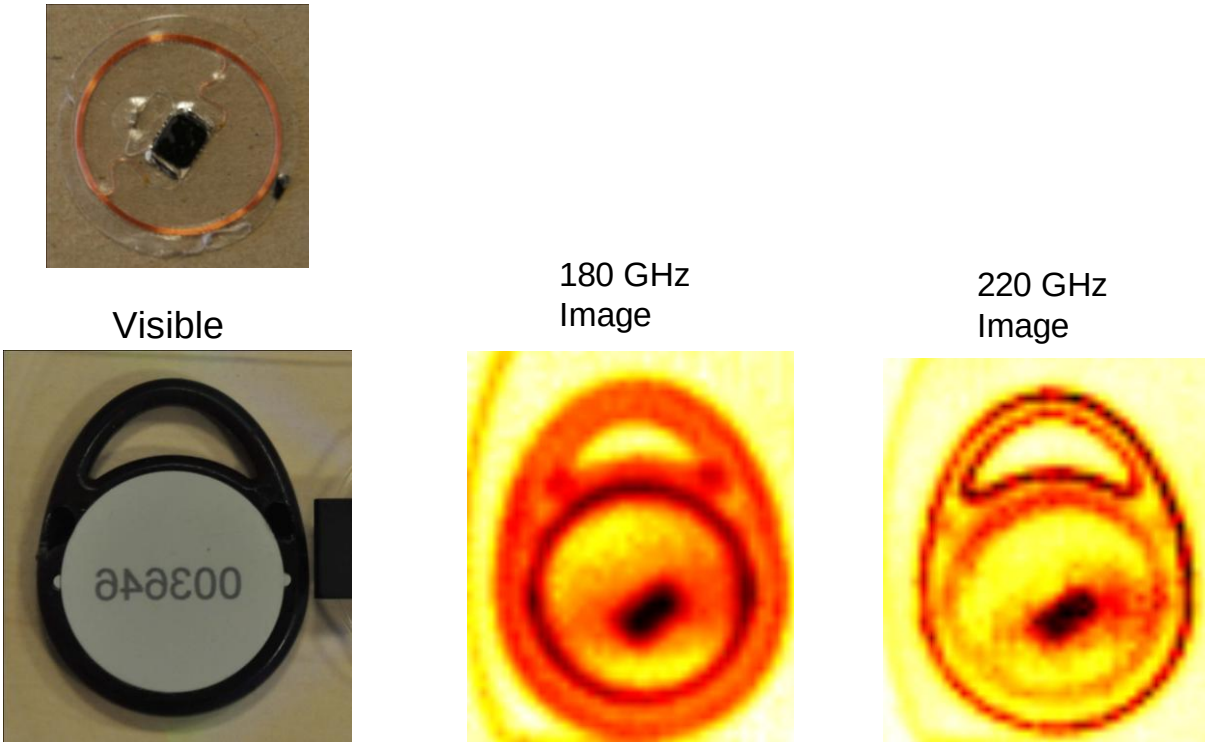

Figure 24 The image of an RFID key has been taken using the 180 GHz and the 220 GHz harmonic generated by the Aleph TX v. 0.3. the images reveal the internal structure of the key as it is clear comparing them with the visible image (top left) of the unpackaged key.

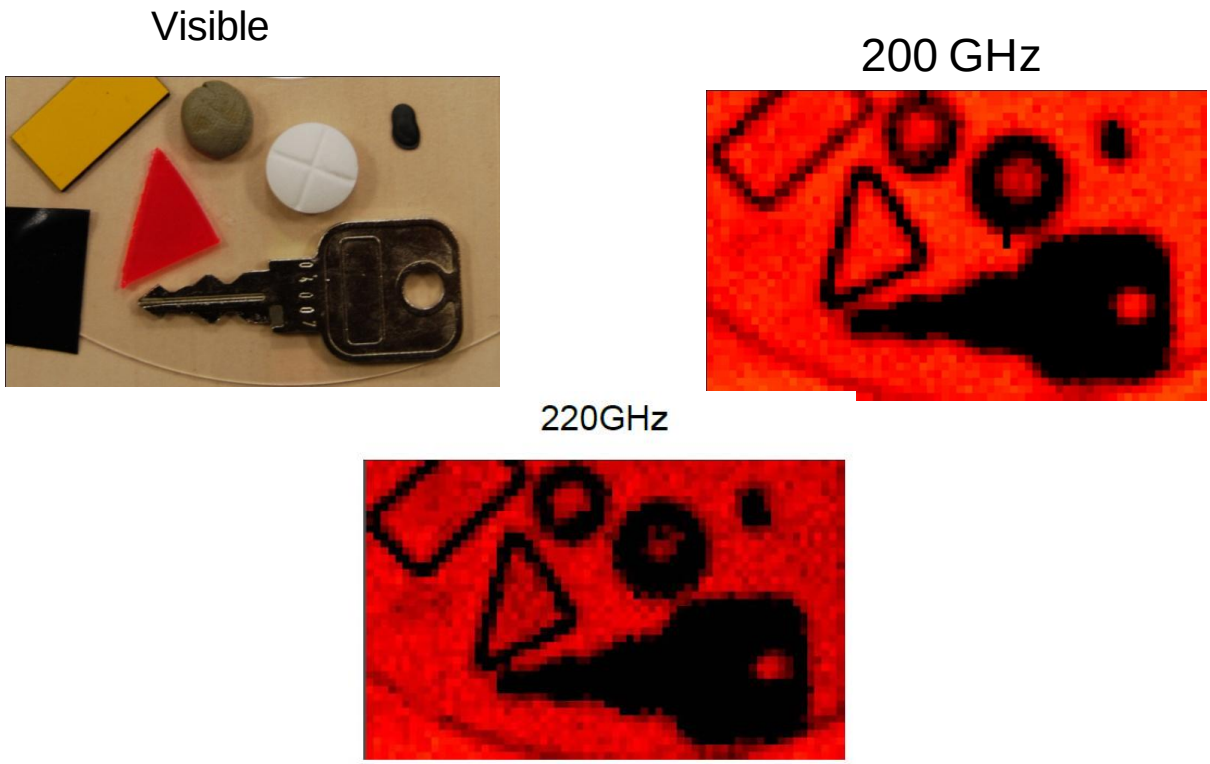

Figure 25 Images of several objects obtained at 200 and 220 GHz compared with the visible image.

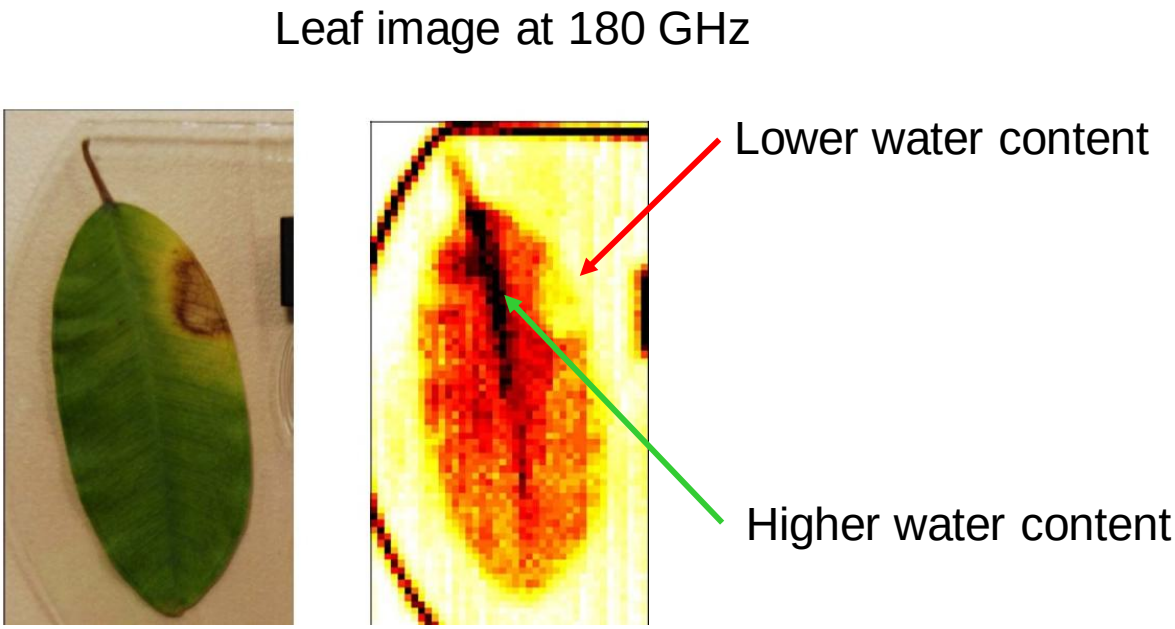

Figure 26 Image of a leaf taken at 180 GHz and compared with its visible counterpart.

6 On-wafer characterization of the final Aleph and Gimel transmitter and receiver

The experimental characterization of the CMOS on-chip sampler is the final step in the validation of the concept of the CMOS integrated circuits for ULTRA. The basic structures, such as the Schottky diodes were experimentally characterized in earlier stages of the project. The design and layout considerations, along with intermediate results were described in detail in former deliverables ([16]-[21]). This deliverable focuses on the characterization of the on-chip transmitter and sampler from the tapeout 3 (TO3) of July 2010.

Various structures have been implemented in tapeout 3 and a full characterization of the sampler and its sub-structures was possible in time as well as in frequency domain.

The results described in this chapter show that the circuit is functional and that the expected behaviour from simulations and calculations is achieved.

One important result is the extraction of the upper frequency limit of the sampler. This is important as it gives the frequency limit of the developed modules. In this deliverable a derivation is given how to extract this limit and it is shown that it exceeds several hundred GHz.

The chapter is structured as follows. In part two the characterization of the transmission lines is presented. These structures are an important part of the sampler layout.

In part three, the characterization of the sampler in time and frequency domain is presented. This section also contains the time-domain characterization of the nonlinear transmission line as this is required for the characterization of the sampler. Also contained in this part is a derivation of the frequency limits of the sampler, as derived from the time-domain analysis. In chapter 4 the spectral analysis of the on-chip nonlinear transmission line with the on-chip sampler is presented. It is shown that spectral components up to 500 GHz were detected with a spectrum analyzer with extreme low noise level.

The successful characterization of the on-chip sampler finalizes the validation of the CMOS part of the ULTRA project.

6.1 Floor plan description

The tapeout 3 of July 2010 contained all required structures for the characterization of the on-chip samplers. It contained the sub-block of the sampler, such as the coplanar waveguides and the slotlines used in the sampler and it contained two types of sampler structures:

1) Sampling structures connected to one NLTL that generates the strobe signal
2) Transmitter-receiver combination: Sampling structure connected to two NLTLs, one for the generation of the strobe signal and one corresponding to the on-chip signal generator.

These structures allow the characterization of the sampler itself and the characterization of the spectrum generated by the nonlinear transmission line based transmitter up to the maximum working frequency of the sampler.

Figure 27 shows a photo of one of the implemented samplers, including the nonlinear transmission line (NLTL) to generate the spikes and the NLTL that generates the signal.

A more detailed photograph of the sampler itself is shown in Figure 28.

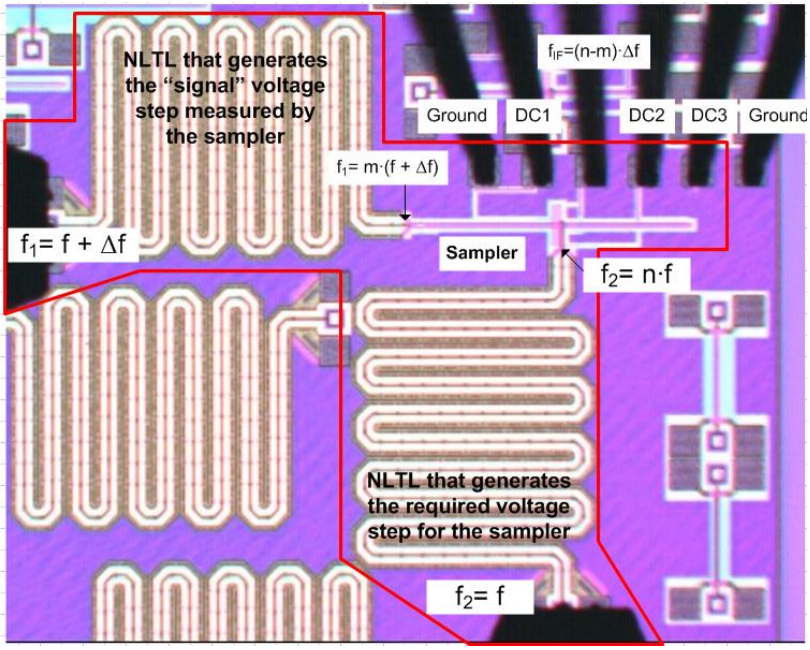

Figure 27 Photograph of the sampler test module. The structure is inside the red polygon. The signal to be sampled by the sampler structure is generated on-chip by a nonlinear transmission line. The input frequency to this line is $f_1=f+\Delta f$. This NLTL will generate higher harmonics at $f_{1out}=n\cdot(f+\Delta f)$. In order to switch the diodes of the sampler, another NLTL is connected to the sampler (from the bottom) that generates a voltage step. The input frequency to this NLTL is $f_2=f$. At the output of this line higher harmonics at frequencies $f_{2out}=m\cdot f$ are generated. Due to the sampler the difference frequencies in the lowest band $f_{IF}=(n-m)\cdot\Delta f$ are generated and received at the IF port of the probe located at the top of the structure.

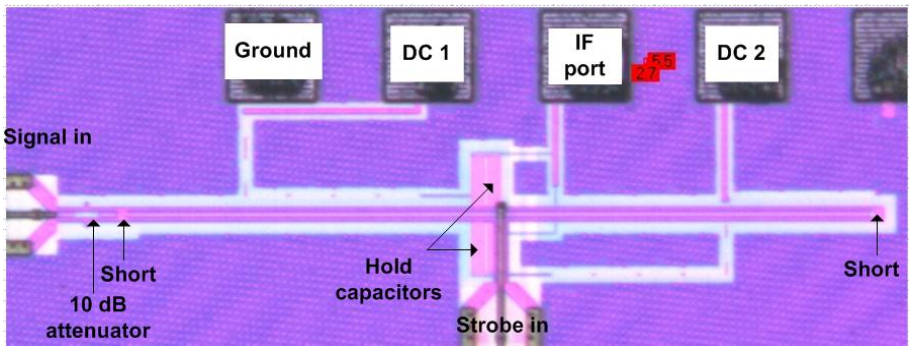

Figure 28 Detailed view of the sampler. The 10 dB attenuator is inserted to reduce the power of the signal to be analyzed by the sampler. On the one hand high power levels in the NLTL lead to the generation of higher powers at the higher harmonic frequencies. On the other hand they might lead to modulation of the bias-setting of the sampler and to undesired mixing products in the sampler.

6.2 Characterization of the transmission lines

As described in previous deliverables, the sampler uses two modes of a three-conductor multi-layer transmission line structure embedded into the CMOS backend layers. As this type of transmission line is new, separate structures for their characterization were added to the tapeout and analyzed.

The layout of the transmission lines used in the sampler is shown in Figure 29.

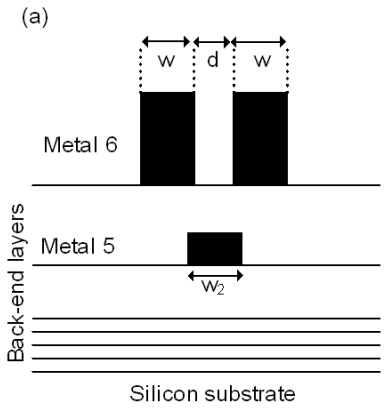

Figure 29 Layout of the transmission used in the sampler. The dimensions are: w=2 µm, d=6 µm and w_2=3 µm.

The transmission lines were characterized with S-parameter measurements up to 67 GHz. The obtained transmission line parameter are shown in Figure 30.

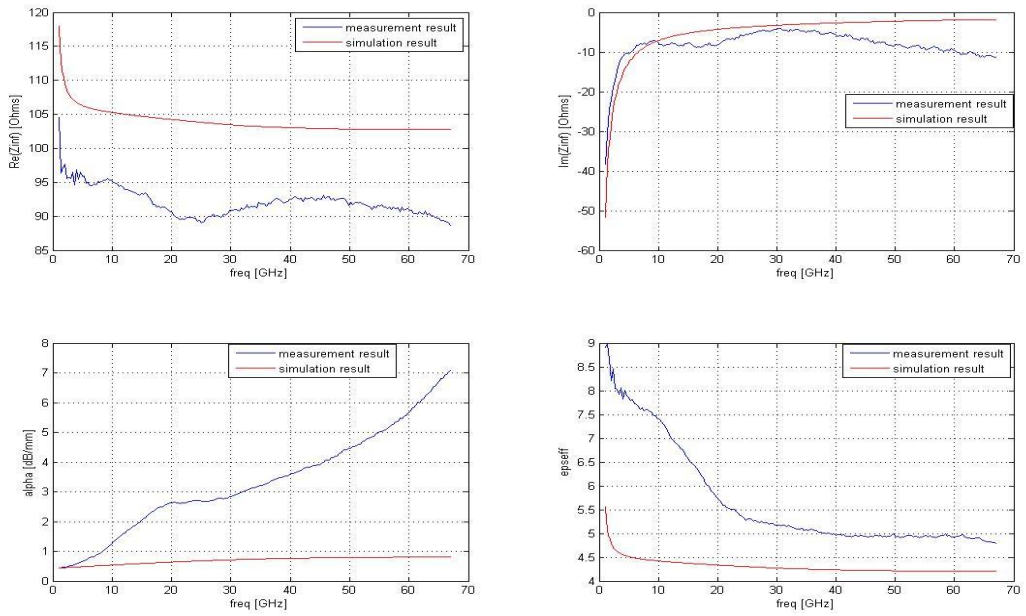

Figure 30 Transmission line parameters of the slotline embedded in the backend CMOS layers.

The impedance of the slotline is about 10 % lower than simulated. This becomes apparent also in the higher value of the effective dielectric constant. The losses of the line are significantly higher than previously simulated. This unexpected high loss has to be corrected for in the measurements of the sampler as it reduces the signal power available for analysis. More detailed simulation of the origin of these losses is required. It might be due to inaccurate modelling of the field penetration into the closely spaced metal lines of the slotline. Above 20 GHz the dispersion of this line is very low, which is important for the propagation of the strobe-signal on these lines. To optimize the sampler performance it is advised to use signal frequencies at above 20 GHz to profit from the low dispersion of the line.

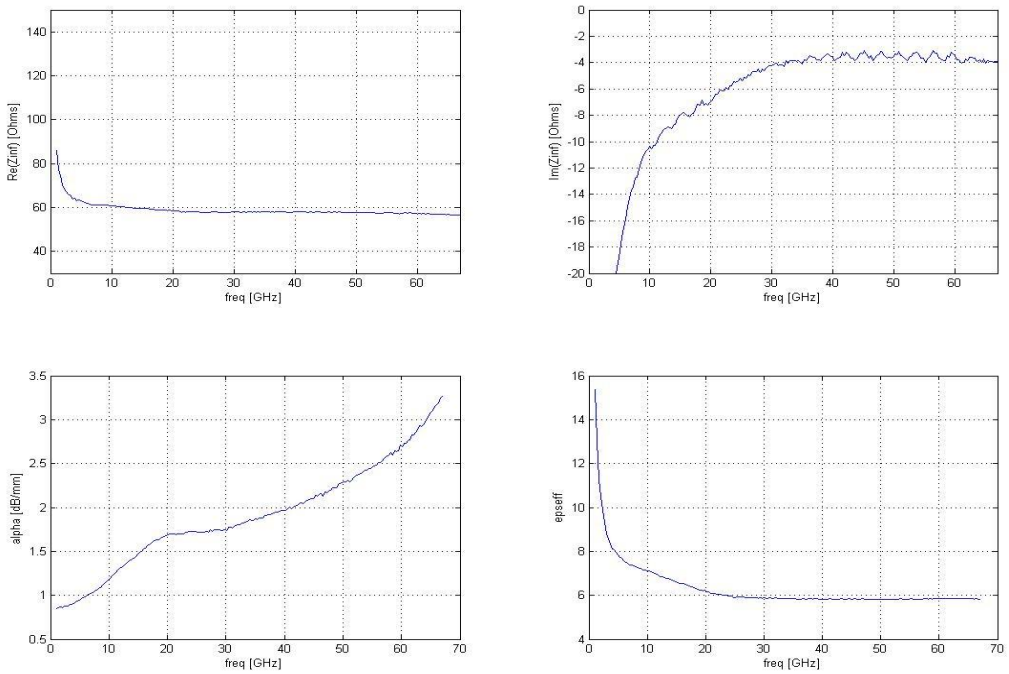

Figure 31 Transmission line parameters of the coplanar waveguide line embedded in the backend CMOS layers.

The coplanar waveguide has a 20 % higher characteristic impedance than expected. The dispersion of this line above 20 GHz is extremely low, which is very important for the characterization of the fast varying signals expected from the nonlinear transmission line. Losses of the coplanar line are higher than expected from simulations. As the length of the CPW line that the signal has to travel is only 300 µm, the effect of the losses is still acceptable. From the low dispersion of the line above 20 GHz it is expected, that the performance of the sampler is best for signals with a bas-frequency above 20 GHz.

6.3 Characterization of the sampler

6.3.1 Limiting frequency of the sampling process

The sampler generates voltage pulses that open and close the two Schottky diodes for a short moment in time. The exact form of these time-dependent diode conductances can only be determined by simulations, including the characteristics of the transmission lines and the diodes. In this paragraphs, the diode conductance is approximated by a triangular shape with a certain pulse width.

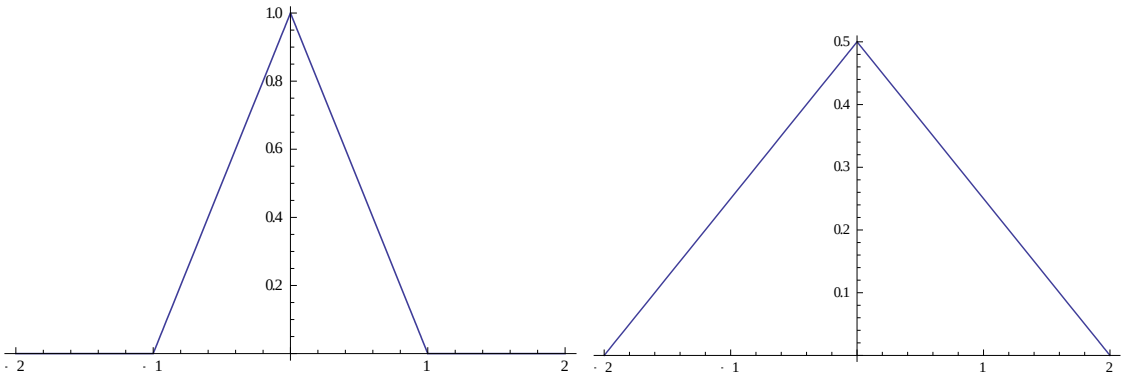

Figure 32 Example of pulse shapes of the generated sampling pulse. The x-axis gives the time in ps, the y-axis the normalized voltage amplitude. The real sampling pulse can only be derived from simulations, taking into account the characteristics of the transmission lines and the diodes.

In time domain the sampled signal s(t) is calculated from the product of the input signal f(t) and the sampling pulse p(t):

$$s(t) = f(t) \cdot p(t)$$

In the frequency domain this corresponds to the convolution of the input signal with the sampling pulse. For an ideal sampling pulse, a delta function, the full frequency content of the input signal is exactly reproduced. For realistic sampling pulses, the spectrum of the sampled signal is limited by the frequency contents and the shape of the sampling pulse.

As an example, the Fourier transformation of the triangular pulses of Figure 32 with a duration of 2ps and 4ps are shown in Figure 33.

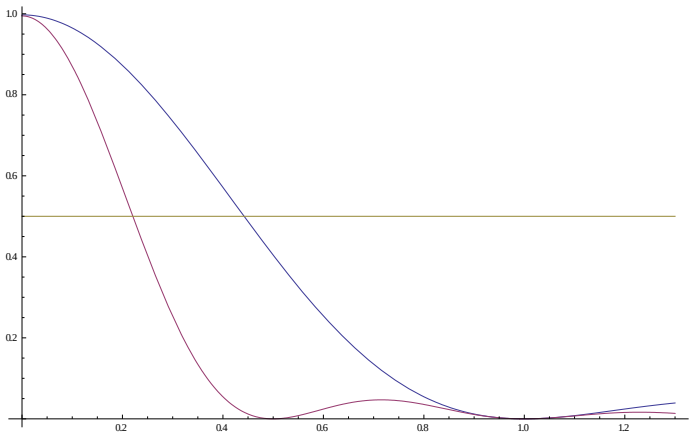

Figure 33 Fourier transformation of the triangular pulses shown in Figure 32. x-axis gives the frequency in THz, y-axis the normalized amplitude

The frequency contents of the sampling pulses used in the sampling circuit differs from the one shown in Figure 33 as a repetitive train of pulses with repetition frequency f_0 is used, e.g. 20 GHz. This repetitive train of pulses is represented by a Fourier series with discrete frequency components, in place of a continuous spectrum. The continuous spectrum shown in Figure 33 gives the envelop of the amplitudes of these components.

If such triangular pulses are used as an approximation of the diode conductance in the sampler, the useful frequency range is determined by:

1) The zero in the Fourier transform of the pulses
2) The minimum voltage/power that can be detected.

To determine the useful frequency range of a sampler, former publications determined the rise/fall-time of the pulse from the measured convolved fall-time of the sampler. They then assumed a certain pulse-envelop with identical rise and fall time and calculated the 3dB bandwidth of the Fourier

transformation of this pulse. Important to realize is, that this is not the practical frequency limit of the sampler. With current spectrum analyzers, extreme low power levels can be measured for noise figures as low as -140 dBm. With an expected signal strength of about -60dBm, the power conversion loss in the sampler can still account for -70 dBm. In a 50 Ω system this corresponds to a voltage attenuation of -35 dB. As a result of the spectral response of the sampler, the dynamic range though will be reduced for higher frequencies. Table 2 shows the theoretical bandwidth of the sampler for pulse widths of 2 ps, 4 ps and 6 ps.

Even for a 6ps pulse width, the 20 dB bandwidth is 302 GHz.

Table 2 Sampler bandwidth at different voltage attenuation levels (reference is the DC level) for a triangular pulse of 2 ps, 4 ps and 6 ps width. Due to the properties of the Fourier transformation, the bandwidth are of course related by a factor 2 and 3 respectively.

	2 ps pulse width	4 ps pulse-width	6 ps pulse-width
3 dB bandwidth	442 GHz	221 GHz	147 GHz
10 dB bandwidth	738 GHz	369 GHz	246 GHz
20 dB bandwidth	908 GHz	454GHz	302 GHz

6.3.2 Time-domain measurement of the sampler and the NLTL

For the characterization of the sampler and the NLTL in time-domain, the structure shown in Figure 27 is used. At the input of the strobe NLTL an 18 dBm signal at 20 GHz is injected. At the input of the signal NLTL an 18 dBm signal at 20 GHz + Δf is injected, with Δf equal to either 1 MHz or 10 kHz. The NLTLs are designed such that they sharpen the falling edge of this sinusoidal signal. The IF output is connected to an oscilloscope and the 90% to 10% fall time is measured. The measured fall-time is then converted back to the original fall-time by multiplying by Δf /20GHz.

An example of such a measurement is shown in Figure 34. It is visible, that the falling edge of the signal is sharper than the rising edge. This shows the pulse-sharpening property of the NLTL.

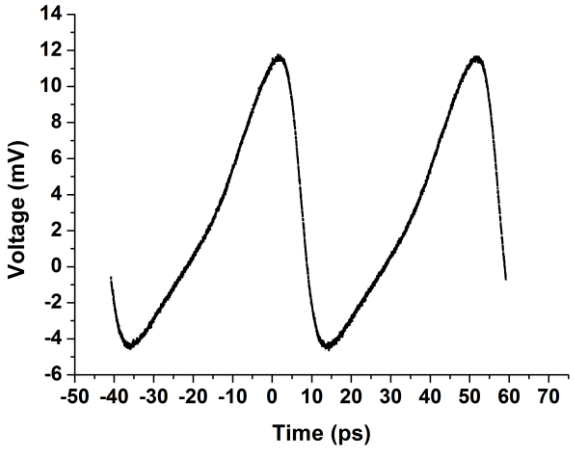

Figure 34 Measured voltage envelope of the IF signal. The time-scale is converted to the original speed of the signal.

The detailed analysis of the fall-time as a function of the diode bias voltage is shown in Figure 35 for the IF frequencies of 10 kHz and 1 MHz.

As a number of resistors are placed in series and parallel to the diode, the actual diode voltage is only a fraction of the voltage applied to the DC pads of the circuit. As expected, the choice of the IF frequency has only a minor influence on the measured fall-times. The measured fall-time is reduced for lower bias voltage at the DC-ports. When the diodes are biased close to the threshhold voltage, the strobe signal forward-biases the diodes for a longer time-interval than in the case that the diodes are

biased at a larger voltage step from the thresh-hold voltage. As the time-interval of forward biasing determines the time-resolution of the sampler, lower bias-voltage enables the measurement of smaller fall-times. At a DC voltage of less than ±6 V, the strobe signal no longer forward biases the diodes.

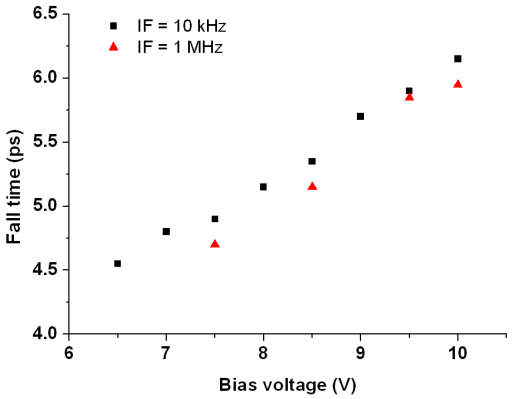

Figure 35 Measurement of the fall time as a function of the DC-biasing for two IF frequencies (IF1=10 kHz and IF2=1 MHz).

The minimum measured fall time of the signal of 4.6 ps is an upper limit for the real fall-time of the NLTL signal. It is the convolved fall-time of the NLTL and the sampler response. With the electro-optical setup at the university of Siegen, the fall-time of the NLTL is measured as 3.5 ps. According to [22], the convolved fall-time is related to the NLTL fall-time and the sampling-circuit rise-time by:

$$T^2_{\text{measured}} = T^2_{\text{sampler}} + T^2_{\text{NLTL}} + T^2_{\text{jitter}}$$

With the assumption of negligible jitter, the known NLTL fall-time of 3.5 ps and the measured fall-time of 4.6 ps, the resulting estimate for the sampler circuit rise time is 3 ps.

From the derivation shown in 6.3.1 it can thus be concluded that the 3 dB bandwidth of the sampler is 147 GHz, the 10 dB bandwidth is 246 GHz and the 20 dB bandwidth is 302 GHz. Figure 36 shows the Fourier transformation of a triangular pulse with 3 ps rise- and 3ps fall time on a logarithmic scale. There is a zero at 333 GHz, which corresponds to the signal period equal to the risetime/falltime. Beyond this frequency, signals can still be detected, until there will be another zero at 666 GHz. There is no principal limit to the sampler. Of course there is the practical limit that power-levels will become too small to be detected.

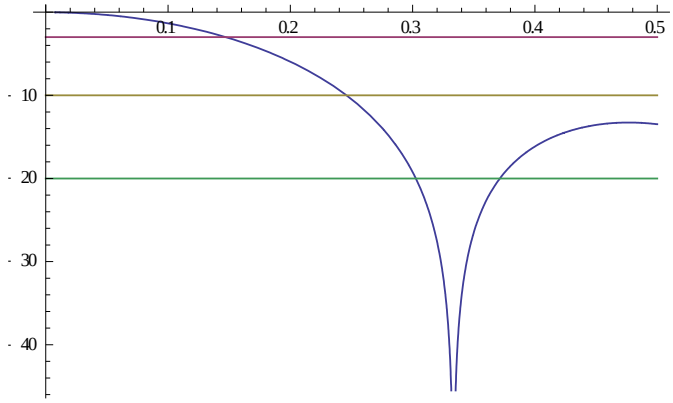

Figure 36 Fourier transformation of a triangular spike with 3 ps rise-time and 3 ps fall-time. The x-axis is the frequency in THz, the y-axis is relative voltage reduction with respect to DC. The horizontal lines indicate the -3dB, -10dB and -20dB bandwidth of the sampler. It also becomes apparent, that frequencies beyond the minimum at 333 GHz, the sampler will give an output power as well.

6.3.3 Characterization of the output spectrum of the sampler

The first characterization of the frequency behaviour of the sampler is done by injecting a signal containing only a single frequency f_0 at a low power level P_0. The strobe signal is shifted with respect to this signal by a small frequency difference Δf and has a high power level P_{strobe}.

The resulting IF frequency spectrum is measured as a function of the voltage bias point of the sampler. The following setting was chosen

Figure 37 shows the result of this measurement for the settings:

f_{strobe}=6.01 GHz P_{strobe}=18dBm

f_{signal}=6 GHz P_{signal}=-10dBm

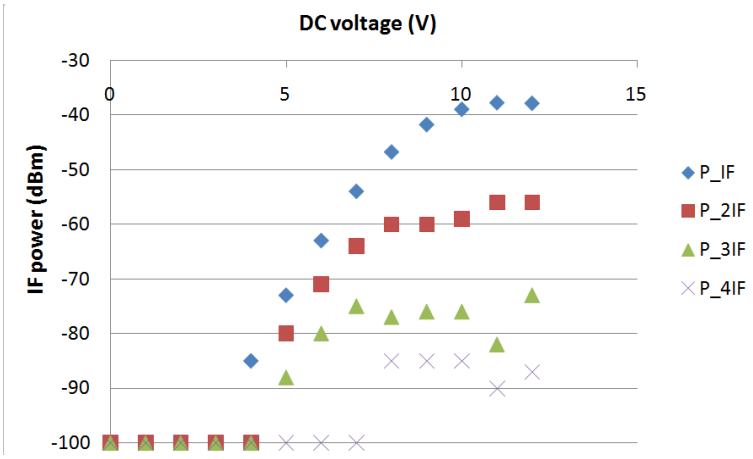

Figure 37 IF power output as a function of the sampler bias voltage. f_{strobe}=6.01GHz, P_{strobe}=18dBm, f_{signal}=6 GHz, P_{signal}=-10dBm.

Furthermore the spectrum outside the IF band was measured with the spectrum analyzer at the 0 V and ±10 V bias of the diode bridge. The measured power levels are shown in Table 2

Table 3 Power spectrum outside the IF band for 0 V and 10 V bias setting and . f_{strobe}=6.01GHz, P_{strobe}=18dBm, f_{signal}=6 GHz, P_{signal}=-10dBm signal power at the signal and strobe input. The yellow first row of the table corresponds to the second harmonic of the signal, all other measured spectral components correspond to the base frequency of the signal.

Frequency (GHz)	Power (dBm) ±10 V bias	Power (dBm) 0 V bias	Frequency component
5,99	-73		$-f_{strobe}+2f_{signal}$
6	-51	-56	f_{signal}
6,01	-38	-37	f_{strobe}
6,02	-64		$2f_{strobe}-f_{signal}$
12,01	-74		$2f_{strobe}+f_{signal}$
12,02	-49,7	-49	$2f_{strobe}$
12,03	-82	-60	$3f_{strobe}-f_{signal}$
18,03	-63		$3f_{strobe}$

The spectral components represent the mixing products that are generated due to the nonlinear behaviour of the sampler. For the final module evaluation, only the IF band is used.

The strobe frequency is multiplied by the nonlinear transmission line, such that the strobe pulse contains all multiples of the initial frequency. The signal input is directly connected to the sampling bridge. Due to the nonlinear conductance of the diodes, the output frequency of the sampler contains:

$$f_{\text{out,sampler}} = \pm n \cdot f_{\text{signal}} \pm m \cdot f_{\text{strobe}}$$

For very weak signals, the main contribution to this frequency spectrum will arise from the component n=1. As it can be seen from Figure 37, there are next to this contribution also spectral components up to the 4th IF frequency, even though there was only a signal at 6 GHz present at the input of the sampler. The power measured for the 2nd to 4th harmonic is generated inside the sampler due to nonlinear modulation of the diode conductance by the 6 GHz signal at the input. These frequency components limit the measurement capability of the sampler to a dynamic range of about 20 dBm for input power level of -10 dBm. In the final measurement, it is expected that the signal received with the antenna will actually have a much lower power level, around -30 dBm to -50 dBm. With these lower power levels, the dynamic range is expected to be larger, as lower power at the higher harmonics will be generated.

Further measurements at lower input power levels should be done to assess the relevance of this nonlinearity at lower input power levels.

The spectral components outside the IF band at 0V bias point contain no further mixing products due to nonlinearities in the sampler. At ±10 V bias point, the first order mixing products are measured next to the basic frequencies put in at the strobe and signal port. The signal at 5.99 GHz reflects also a second order mixing product generated inside the sampler. This frequency corresponds to the second harmonic of the input signal mixed with the strobe signal. This also reflects the non-linear modulation of the diode conductance with the signal-power.

The conversion efficiency for various signal levels at different harmonics was characterized. Therefore a sine-signal of frequency nf_0 with power levels between -20 dBm and 5 dBm was injected into the signal port of the sampler, for several values of n. The strobe signal of $f_0+\Delta f$ was injected at the strobe port.

Figure 38 shows the IF power spectrum for the case f_{signal}=n·6GHz and n equal to 1, 5 and 11. For signal powers up to -5 dBm the IF power follows linearly with a conversion efficiency of -30 dB for the first harmonic, of -55 dB for the 5th harmonic and of -70 dB for the 11th harmonic. Higher harmonics could not be measured due to the maximum frequency of 67 GHz available from the signal generator.

As shown in Figure 38, the conversion efficiency decreases linearly with the harmonic number by about 3dB per harmonic. Compared to the generation of second, third and forth harmonic by nonlinear processes inside the sampler as shown in Figure 37, the dynamic range is about 17 dBm at 10 V bias point setting.

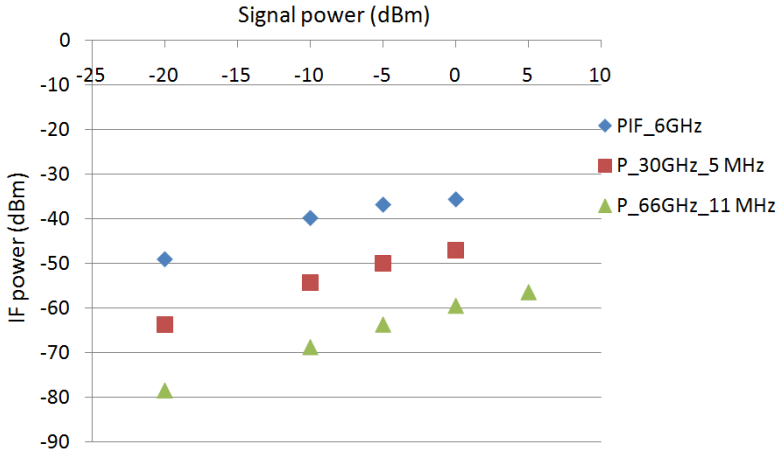

Figure 38 Output power spectrum at IF frequency for f_{strobe}=6.001 GHz, P_{strobe}=18dBm, f_{signal}= n × 6.0 GHz (with n equal to 5 and 11).

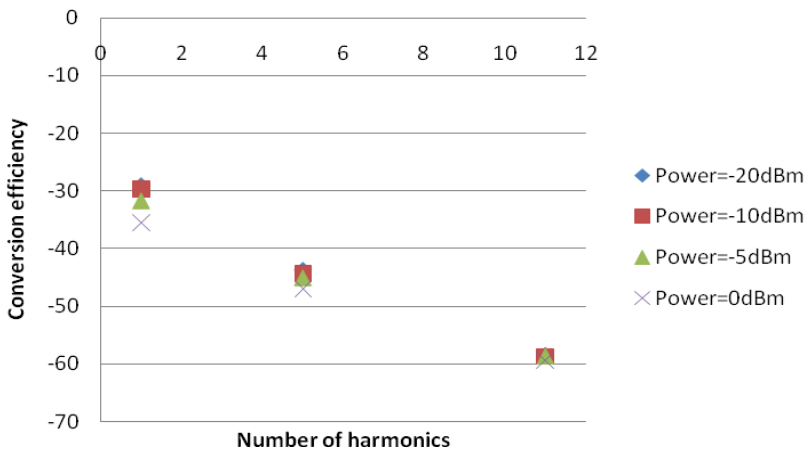

Figure 39 Conversion efficiency at the 1st, 5th and 11th harmonic of 6 GHz for input power levels between -20 dBm and 0 dBm, measured for sampler setting of for f_{strobe}=6.001 GHz, P_{strobe}=18dBm, Vbias=±10 V.

Output power for higher input frequencies is shown in Figure 40. For signal levels up to -5 dBm, the conversion efficiency is linear. The low-input power range is the important range for our system.

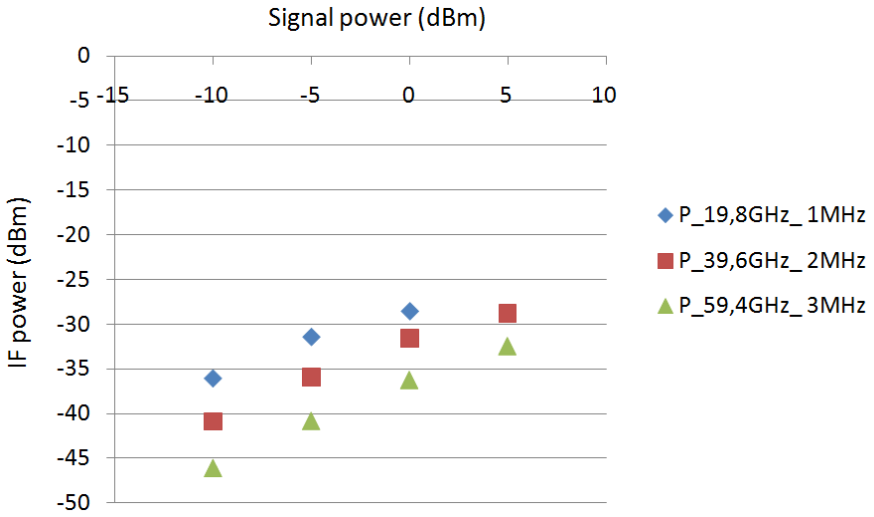

Figure 40 Output power spectrum at IF frequency for f_{strobe}=19.801 GHz, P_{strobe}=18dBm, f_{signal}= n × 19.8 GHz (with n equal to 1,2 and 3).

6.4 Characterization of the NLTL output spectrum

The output spectrum of the NLTL was characterized on-chip with the structure shown in Figure 27. In this structure, the input signal of the sampler is the output power generated by the on-chip NLTL. In the final module, the signal will be received by an antenna. The measured output spectrum is shown in Figure 41. The measurement of the IF output power is performed with a spectrum analyzer with a noise level of -140 dBm for 1 Hz measurement bandwidth.

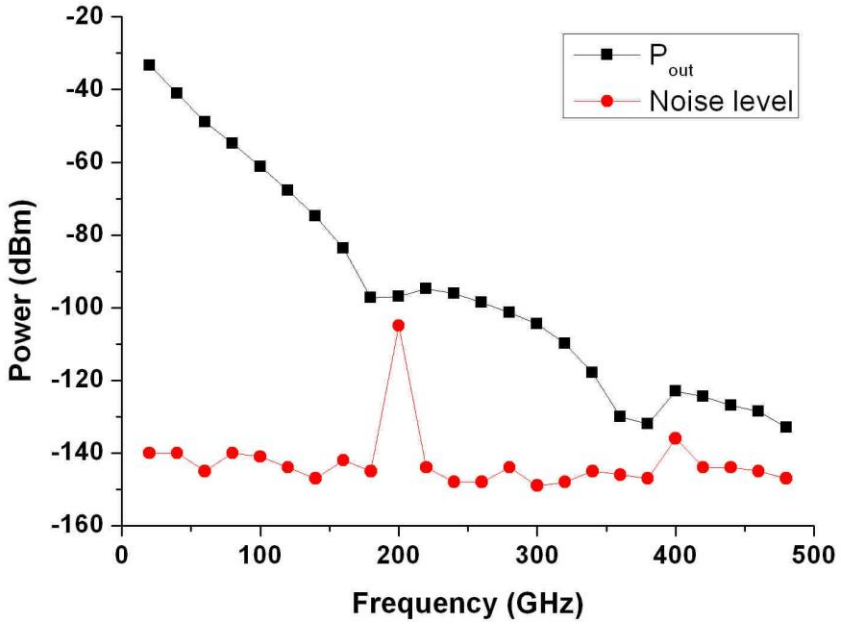

Figure 41 Output spectrum of the NLTL, as measured with the on-chip sampler at IF frequency. The input signal is at f=20 GHz with 18 dBm of power, the frequency offset is Δf = 1 MHz. Due to the on-chip attenuator, the power of the signal is about 10 dB smaller than the power of the strobe at the input of the sampler. The minimum at 360 to 380 GHz corresponds to the minimum of the Fourier transformation of the sampling pulse. The variation in the slope of the curve at 180 GHz might be due to the NLTL output spectrum.

Up to 180 GHz the power decreases linearly. At 360 GHz to 380 GHz there is a minimum in the curve, which reflects the transfer function of the sampler as described in the previous paragraph. Slight increase in the output power, such as at 200 GHz and 220 GHz were also seen in simulations of the NLTLs.

As explained in the previous paragraph, there is no hard frequency limit of the sampler, but the limit is given by the minimum measurable signal power. This is in the current measurement the noise-level of around -140 dBm. The higher noise-power measured at 200 GHz and 400 GHz might be due to resonances in the sampler structure.

7 Conclusions

This deliverable reports several intermediate measurement results of the ULTRA project.

In chapter 2, the Aleph/Gimel transmitter version 0.1 (composed of the NLTL fabricated with TO1 and an on-chip antenna) is characterized. The device show functionality and the measurements have demonstrated its capability to generate extremely wide-band signals up to 160 GHz. The on-chip antenna has been characterized also separately from the NLTL. On-wafer measurement has been conducted to measure the return loss and gain of the EWB antenna. The antenna demonstrated an extremely wide band performance in the range of 120 GHz ~ 350 GHz, experimentally verified in the range of 220 GHz ~ 300 GHz. The simulated antenna pattern showed an omnidirectional radiation characteristic, and the antenna gain which was retrieved from the measured output power was in good agreement with simulations.

In chapter 4, the Aleph/Gimel transmitter version 0.2 (composed of the NLTL fabricated with TO1 and an off-chip Vivaldi antenna) is characterized. Measurements of the module have demonstrated its capability to generate extremely wide-band signals up to at least 170 GHz and with a total emitted power of around -35 dBm at 150 GHz when an input signal at 10 GHz with a power of 18 dBm is provided. The nonlinear transmission line has been tested alone with input signals at 6 and 10 GHz and is able to generate a broadband signal from 6 GHz to 170 GHz at least with a power of around -30 dBm at 150 GHz and -37 dBm at 170 GHz when its input signal is at 10 GHz and has a power of 18 dBm. The off-chip Vivaldi antenna shows directive radiation pattern in the whole measured band of 90-150 GHz and simulations show an efficiency of 70%. A comparison of the transmitters version 0.1 and 0.2 indicates that the approach with the off-chip Vivaldi antenna (version 0.2) has superior performance. For this reason and also to minimize expensive CMOS area such an approach has been chosen for the final demonstrators.

In chapter 5, the Aleph/Gimel transmitter version 0.3 (basically identical to version 0.2) has been used to generate thru the package images of an RFID key and images of a leaf and a set of other small objects. The images were taken at frequencies up to 220 GHz. The maximum frequency was limited by the commercial receiver available in the laboratory for the test. It is expected that the ULTRA receiver will allow not only imaging, but also spectroscopy beyond 220 GHz.

In chapter 6 the on-chip sampler (TO3), which is the last part of the CMOS circuits required for the final system validation, is characterized. It was shown that the samplers is functional up to several hundred GHz. Based on the time-domain measurements of the NLTL output signal, a sampler rise and fall-time of 3 ps was derived. This value was related to the sampler frequency domain response. The 3 dB bandwidth of the sampler is 147 GHz, the 10 dB bandwidth is 246 GHz and the 20 dB bandwidth is at least 302 GHz. Depending on the noise-level of the spectrum analyzer, more bandwidth is possible. Experimentally, higher harmonics of the output spectrum of the meandered nonlinear transmission line up to 500 GHz were detected. The sampler and the nonlinear transmission line implemented in TO3 will be packaged to create the final Aleph/Gimel transmitter and receivers.

8 References

[1] J.S. Bostak et al., “All-electronic terahertz spectroscopy system with terahertz free-space pulses,” J. Opt. Soc. Am. B 11, No. 12, 2561-2565 (1994).

[2] Y. Konishi et al. “Picosecond electrical spectroscopy using monolithic GaAs circuits,” Appl. Phys. Lett. 61 (23), 7 December (1992).

[3] M.J. Rodwell et al., “GaAs Nonlinear Transmission Lines for Picosecond Pulse Generation and Millimeter-Wave Sampling,” IEEE Trans. Microwave Theory and Tech. 39, No. 7, 1194-1204, July 1991

[4] T. S. Dickson and J. R. Long, “Shielded Passive Devices for Silicon-Based Monolithic Microwave and Millimeter-Wave Integrated Circuits”, IEEE J. Solid State Cir. 41, No. 5, May 2006

[5] W. R. Eisenstadt and Y. Eo, “S-parameter-based IC interconnect transmission line characterization”, IEEE Trans. On Comp., Hybrids, and manufacturing Tech., vol. 15, No. 4, Aug. 1992

[6] Yu, R.Y., et al., “275 GHz 3-Mask Integrated GaAs Sampling Circuit”, Electronics Letters, 1990. 26(13): p. 949-950.

[7] Case, M.G., Nonlinear Transmission lines for Picosecond Pulse, impulse and millimeter-wave harmonic generation, in Electrical and Computer Engineering. 1993, University of California: Santa Barbara.

[8] Zeland, IE3D version 10.

[9] Colvin, J.T., S.S. Bhatia, and K.O. Kenneth, Effects of substrate resistances on LNA performance and a bonpad structure for reducing the effects in a Silicon Biploar Technology. IEEE Journal of solid-state circuits, 1999. 34(9): p. 1339-1344.

[10] Kolding, T.E., Shield-based microwave on-wafer device measurements. IEEe Transaction on Microwave Theory and Techniques, 2001. 49(6): p. 1039-1044.

[11] Goldfarb, M.E. and R.A. Pucel, Modelling Via hole grounds in microstrip. IEEE Microwave and guided wave letters, 1991. 1(6).

[12] Wartenburg, S.A., RF measurement of die and packages. 2002: Artech House.

[13] Publications and Patents by microTEC, e.g. (3D-CSP) Microsystem technology Process Patent 199 64 099 and PCT/DE00/04393, Dec. 31, 1999; www.microtec-d.com.

[14] R. Götzen, “Verfahren zur Produktion von Hochfrequenz Leiterbahnen deren Ankopplungen an Bauelementen wie Halbleiter Bauelemente, Antennen, koaxial Kabeln und Hohlleiter,” German Patent 10 2010 053 047.6, 2010.

[15] R. Götzen, “Die Freiheit der werkzeuglosen Fertigung,” Mikroproduktion, pp. 47-50, Feb. 2008.

[16] L. Tripodi, et al., Lab-on-chip terahertz spectroscopy system with plasmonic sensor patent filing number PH011627EP1/EPO08170053.6 2007, Philips: Nederland.

[17] M. Matters et al, “RF characterization of Schottky diodes in 65nm CMOS,” IEEE Tran. on Electron Devices, **57**(5), pp. 1063-1069, May 2010.

[18] L. Tripodi et al., “First design and layout of the NLTL, driving circuitry, sampling head and antenna,” ULTRA project deliverable D2.2.

[19] L. Tripodi et al., “Building blocks of an integrated spectrometer: First design and layout of NLTLs, sampling head and antenna,” Philips Technical Note TN2009/479.

[20] L. Tripodi et al., “Evaluation of varactors and a Schottky diode in 65-nm CMOS for potential THz applications,” Philips Technical Note TN2008/00632

[21] L. Tripodi et al., “2nd design and layout of the NLTL, driving citcuitry, sampling head and antenna”, ULTRA project deliverable D2.4.

[22] R. Y. Yu et al., 275 GHz 3-mask integrated GaAs sampling circuit, Electronics letters, Vol. 26, no. 13, 1990.